Gene network involved in the development of multidrug resistance in *Klebsiella pneumoniae*

Hyunsook Lee

The Graduate School
Yonsei University
Department of Medical Science

Gene network involved in the development of multidrug resistance in *Klebsiella pneumoniae*

A Dissertation Submitted
to the Department of Medical Science
and the Graduate School of Yonsei University
in partial fulfillment of the
requirements for the degree of
Doctor of Philosophy in Medical Science

Hyunsook Lee

June 2024

This certifies that the Dissertation of Hyunsook Lee is approved.

Thesis Supervisor	Dongeun Yong
Thesis Committee Member	Hyukmin Lee
Thesis Committee Member	Sang Sun Yoon
Thesis Committee Member	Insuk Lee
Thesis Committee Member	Moo Suk Park

The Graduate School
Yonsei University
June 2024

ACKNOWLEDGEMENTS

Dr. Chungsik Choi of BD & FAS explained and educated me about RT-qPCR, covering both theoretical and experimental aspects. Gyusik Kim, a bioinformatician from MolCube in Seoul, South Korea, addressed molecular docking issues and gave advice on preparation for MD simulations. Professor Wonpil Im of Lehigh University, Pennsylvania, USA, gave me an excellent opportunity to learn about molecular docking interactions and MD simulation analysis. Johnathan Lin, a graduate student at National Sun Yat-sen University's College of Medicine in Kaohsiung, Taiwan, advised me and did MD simulation analysis. Professor Sung-Huan Yu of the National Sun Yat-sen University College of Medicine in Kaohsiung, Taiwan, provided invaluable guidance on the key portions. My advisor, Professor Dongeun Yong has been an amazing source of support and direction for me throughout the years, keeping me on track. Professors Hyukmin Lee, Sang Sun Yoon, Insuk Lee, and Moo Suk Park gave me insightful guidance. Finally, my mother has been inspiring and strengthening me all year to pursue my passion.

TABLE OF CONTENTS

LIST OF FIGURES

LIST OF TABLES

ABSTRACT

Gene network involved in the development of multidrug resistance in *Klebsiella pneumoniae*

The development of novel drug classes to treat multidrug-resistant bacteria has become limited since the 1980s, underscoring the urgent need for innovative antibiotics. The growing death rate due to antibiotic resistance currently outnumbers other major illnesses, making it a serious global health problem. Bacterial evolution has advanced with the introduction of authorized antibiotics by the Food and Drug Administration, aggravating the antibiotic resistance dilemma and generating considerable financial losses to the medical care system.

This study aims to identify potential targets and promising compounds by comparing previous experimental results with bioinformatical and computational methods. The adoption of a combinational approach is proposed as an option to tackle the impact of diseases on global public health by preventing breaking the balance among humans, animals, and nature. Repurposing or partially repurposing current medications provides another unique method with a broad spectrum, a lower risk of resistance development than monotherapy, and efficacy against a

wide range of strains. Furthermore, using lower therapeutic dosages reduces adverse effects and improves effectiveness.

One of the ESKAPE pathogens, *Klebsiella pneumoniae*, can cause infections both in hospitals and in the community. In this study, the diverse pathways, characterized by particular gene expression, contribute to the combination therapy mode of action and bacterial survival mechanisms. The computational ANNOgesic tool detects the linkages (noncoding RNAs) that make up a functional network of pathways. In post-transcriptional regulation, regulatory RNA components like riboswitches and RNA thermometers charge an adaptive bacterial response to harsh environmental circumstances. The research also discovered the existence of novel small regulatory RNAs that has connection with target genes and their related genes. These findings will help in finding promising antimicrobial alternatives to treatment. Overall, this study sheds light on the synergistic chemical substances and antibiotics effects, stressing the significance of regulatory RNA elements in responses of bacterial survival.

Filtering candidate chemical compounds to locate hit compounds and considering potential analog compounds will expand the range of options for future research. Furthermore, we phased in the molecular dynamics simulation to study the complex system's reaction to perturbed conditions through the physical movements of biomolecules. However, 10 ns MD simulations do not allow enough time for system equilibrium and protein-ligand complex convergence. Increasing confidence in screening candidate compounds necessitates 200 ns MD simulations and MM-PBSA (Molecular Mechanics Poisson-Boltzmann Surface

Area) or MM-GBSA (Molecular Mechanics Generalized Born Surface Area) binding free energy calculation. In the future, the area of inquiry will be broadened to encompass not only the identification of hit compounds, but also the discovery of related compounds. More research is required in synthetic biology, pharmacology, and biotechnology. This study makes a fundamental proposal for a solution to antibiotic resistance.

Key words : multidrug-resistant, meropenem, colistin, synergy, ANNOgesic, noncoding RNA, gene network, protein and ligand interaction, cheminformatics, molecular dynamics simulation

1. Introduction

Infection of Gram-negative *Klebsiella pneumoniae* can cause a variety of conditions, including urinary tract infections, bloodstream infections, pneumonia, cellulitis, intra-abdominal infections, pyogenic liver abscesses, and meningitis[1]. This encapsulated, non-motile bacteria poses a global hazard to public health due to its hypervirulence and antibiotic resistance.
Previous research has focused on K56's reaction to meropenem therapy as well as colistin resistance mechanisms[2]. The investigations used transcriptome analysis, complementation, and knockout approaches to identify both agonists and antagonists linked with antibiotic meropenem. Creating novel medications and specifically knocking out genes for therapeutic purposes has been challenging due to many hurdles.

Strain K56, unlike its parent strain K26, is resistant to multiple drugs, including carbapenem[2] and colistin, after meropenem therapy. The transition from sensitivity to resistance to meropenem and colistin was seen throughout dosing. K56 is a multidrug-resistant strain with sequence Type 11, but there are neither carbapenemase production[2] nor colistin-related resistance genes found in the DNA (Table 1)[3].

K56 demonstrates adaptive tolerance to stress, including extreme environmental conditions[4]. Meropenem was used in in vitro tests to screen a library of 6,696 compounds. Six chemicals showed synergistic effects

against K56. However, none of the compounds demonstrated antibacterial action at lower doses. Only chemical #3 eventually had an additive interaction with meropenem. The last-resort antibiotic colistin was evaluated for susceptibility, and candidate chemical #3 was found to be synergistic with colistin (Figure 2).

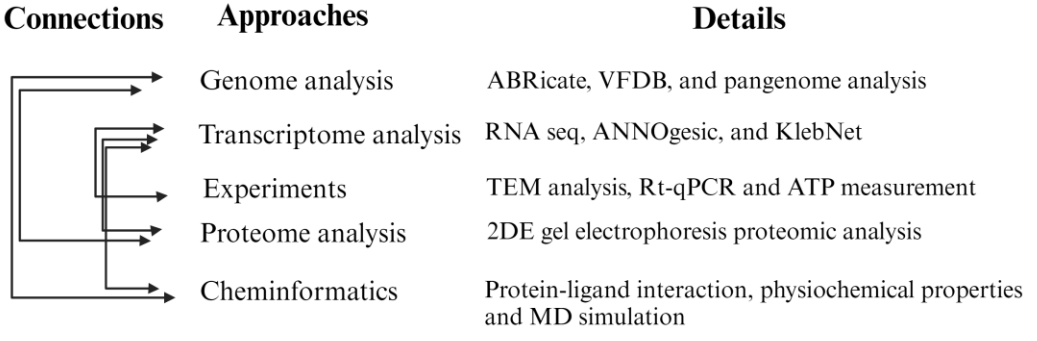

Figure 1. Summary of relationships between sub-chapters.

Table 1. ResFinder's K56 resistome data

Database	Resistance gene	Identity	Query / Template length	Contig	Position in contig	Accession number
aminoglycoside	*aadA2b*	99.87	780 / 780	NODE_54_length_2222_cov_35.268258	1082..1861	D43625
aminoglycoside	*aph(3'')-Ib*	100	803 / 804	NODE_44_length_6725_cov_8.216884	4935..5737	AF024602
aminoglycoside	*aph(3'')-Ib*	99.88	804 / 804	NODE_44_length_6725_cov_8.216884	4935..5738	AF313472
aminoglycoside	*aph(3'')-Ib*	99.88	804 / 804	NODE_44_length_6725_cov_8.216884	4935..5738	AF321550
aminoglycoside	*aph(3'')-Ib*	99.88	804 / 804	NODE_44_length_6725_cov_8.216884	4935..5738	AF321551
aminoglycoside	*aph(6)-Id*	100	837 / 837	NODE_44_length_6725_cov_8.216884	4099..4935	M28829
aminoglycoside	*armA*	100	774 / 774	NODE_40_length_10812_cov_10.040618	6564..7337	AY220558
beta-lactam	blaDHA-1	100	1140 / 1140	NODE_49_length_3781_cov_8.855227	1434..2573	Y16410
beta-lactam	*bla*SHV-12	100	699 / 861	NODE_77_length_722_cov_75.137815	1..699	KF976405
beta-lactam	*bla*SHV-129	100	699 / 861	NODE_77_length_722_cov_75.137815	1..699	GU827715
beta-lactam	*bla*SHV-13	100	699 / 861	NODE_77_length_722_cov_75.137815	1..699	AF164577
beta-lactam	*bla*SHV-155	100	699 / 858	NODE_77_length_722_cov_75.137815	1..699	JX121122
beta-lactam	*bla*SHV-172	100	699 / 861	NODE_77_length_722_cov_75.137815	1..699	KF513177
beta-lactam	*bla*SHV-31	100	699 / 861	NODE_77_length_722_cov_75.137815	1..699	AY277255
fosfomycin	*fosA*	99.27	412 / 420	NODE_16_length_124455_cov_28.116860	14077..14488	ACWO01000079
macrolide	*mdf(A)*	80.16	1144 / 1233	NODE_2_length_536394_cov_28.662023	226305..227443	Y08743
macrolide	*mph(E)*	100	885 / 885	NODE_40_length_10812_cov_10.040618	1850..2734	DQ839391
macrolide	*msr(E)*	100	1476 / 1476	NODE_40_length_10812_cov_10.040618	2790..4265	FR751518
quinolone	*oqxA*	100	1176 / 1176	NODE_1_length_644183_cov_29.464017	30796..31971	EU370913
quinolone	*oqxB*	100	3153 / 3153	NODE_1_length_644183_cov_29.464017	31995..35147	EU370913
sulphonamide	*sul1*	100	840 / 840	NODE_50_length_3063_cov_31.185286	1954..2793	U12338

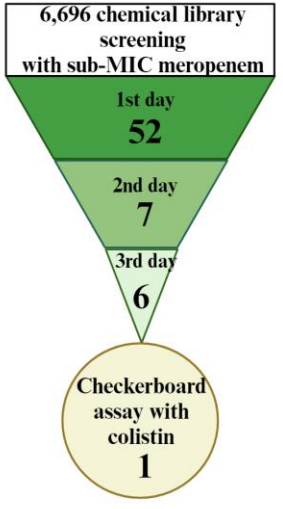

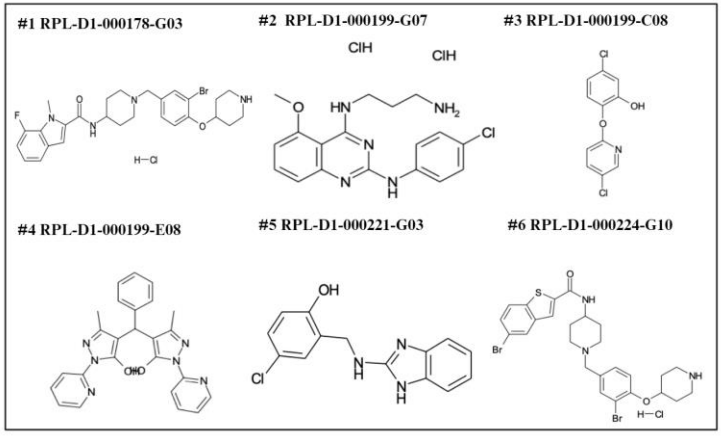

Figure 2. Screening a library of 6,696 chemical compounds. Meropenem was screened at a sub-MIC concentration of 8 μg/ml against the multidrug-resistant bacteria K56. Following three days of observation, six candidates with synergistic activity were identified. K56's susceptibility to six compounds coupled with meropenem was tested using a checkerboard assay. Only chemical #3 (RPL-D1-000199-C08) had an additive effect with meropenem. Chemical #3 was tested with colistin, and strain K56 remained responsive. Triclosan and meropenem showed synergy when evaluated alongside 1,142 similar compounds under identical conditions.

This study aimed to reduce the negative impact of multi-drug-resistant Klebsiella pneumoniae on community health while also promoting ecological harmony between humans, animals, and their environment. This research sought to investigate the synergistic therapy between chemical compounds, meropenem, and colistin.

A broad-spectrum β-lactam meropenem binds to penicillin-binding proteins and then inhibits the formation of cell wells. A polymyxin E, colistin, reacts with lipopolysaccharides and phospholipids, disrupting the outer membrane, raising cell permeability, and causing cell lysis as well as death[5]. Colistin monotherapy can induce severe consequences, including nephrotoxicity and neurotoxicity[6]. Combining colistin with other antibiotics could be effective against multidrug-resistant Gram-negative bacteria[7].

Chemical #3 from the 6,696 chemicals library is comparable to triclosan. Triclosan inhibits the biosynthesis of fatty acids by binding to the enzyme FabI (enoyl-acyl carrier protein reductase). It affects phospholipids, lipopolysaccharides, and lipoprotein production. Both colistin and triclosan cause cell surface stress in bacteria. The mechanism of chemical #3's synergistic interaction with colistin remains unknown.

Both phenotypic and genotypic approaches can reveal hidden elements of the K56 strategy. Transcriptome analysis has recognized that differentially expressed genes (DEGs) serve in resistance and treatment processes. ANNOgesic was utilized to examine K56's features following the combo

treatment. Genome annotation systems, like Prokka and EuGene-PP, rely on a reference genome, which may not accurately represent real-world experimental settings. ANNOgesic tool can predict the characteristics of over 20 bacterial genomics grounded in RNA-Seq (https://github.com/Sung-Huan/ANNOgesic). This modular software optimizes parameters and eliminates false positives to ensure the quality of results[8]. ANNOgesic analysis can identify affected genes by analyzing regulatory RNAs such as RNA thermometers, riboswitches, and small regulatory RNAs (sRNAs). Regulatory RNAs play a variety of roles in biological functions, developmental metabolism, and pathogenesis[9]. They can improve combination treatment efficacy and reduce fitness in constrained settings, helping battle antibiotic resistance[10].

To study the post-translational modification, the proteins were separated and then identified with two-dimensional (2DE) gel electrophoresis and mass spectrometry (MS)[11]. The isoelectric point and size of discrete complex proteins[12] are determined. Quantified proteins determine unknown biomolecules through mass-based detection[13]. This high-throughput and high-resolution technique defined the protein expression level of the identical protein spots in each different treatment condition.

The final section of this chapter focuses on the cheminformatics perspective. Cheminformatics combines computational and informational techniques to convert chemical data into knowledge[14] for drug discovery. This computer-aided strategy saves time, funds, and effort while searching

for potent chemical compounds. This work uses cheminformatics to predict molecular docking at active sites and analyze potential treatments. Cheminformatics can determine protein-ligand interactions, physicochemical features, and similarity comparisons. These determinations are critical in drug development investigations. To assure the acquisition of entire genetic variants[15] among extremely similar strains with vertical relationships, a pangenome study is used to concentrate on genomic evolution[16]. The investigation identified a gene that is present in only one strain but not in another. Bioinformatic approaches, including alignment and systems biology tools, helped define the target[17].

At the end, molecular dynamics (MD) simulation was brought in to gain a deeper understanding of the mechanism and biological function[18]. MD gives us not only the characteristics of protein-ligand complex systems[19] but also the binding energy of protein-ligand interactions[20].

2. Materials and Methods

2.1. Genome analysis at the DNA level

2.1.1. DNA extraction

Whole genome sequences (MiSeq) were prepared with Wizard® Genomic DNA purification kit from Promega (Promega, Madison, WI, USA). All procedures were based on the manufactural protocol.

2.1.2. Genomic visualization tools

Bioinformatics Application for Navigating *De novo* Assembly Graphs Easily (Bandage)[21], and BLAST Ring Image Generator (BRIG)[22] tools allowed pangenome, and genomic comparison visualization.

2.1.3. Mass screening of contigs for antimicrobial resistance and virulence factors

ABRicate (https://github.com/tseemann/abricate) detected antimicrobial resistance genes and virulence factors of pathogenic bacteria from the DNA assemblies with the NCBI database.

2.2. Transcriptome analysis at the RNA level

2.2.1. Screening the chemical compounds library

To assess the impact of chemicals on K56, was exposed to sub-MIC meropenem (8 μg/ml) and a library of 6,696 chemicals from the Korea

Chemical Bank. The broth microdilution technique was used for synergistic screening, in accordance with Clinical and Laboratory Standards Institute guidelines. A total of 1,142 chemicals from the similar source were screened. All compounds were subjected to the same experimental technique (Figure 3 and Figure 4).

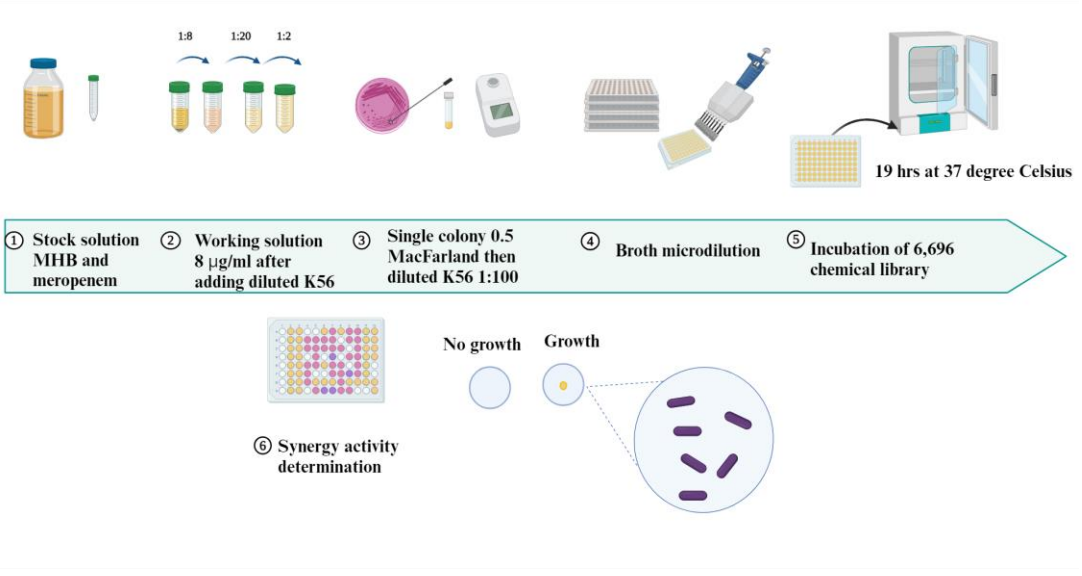

Figure 3. Broth microdilution procedure for phenotypic characterization.

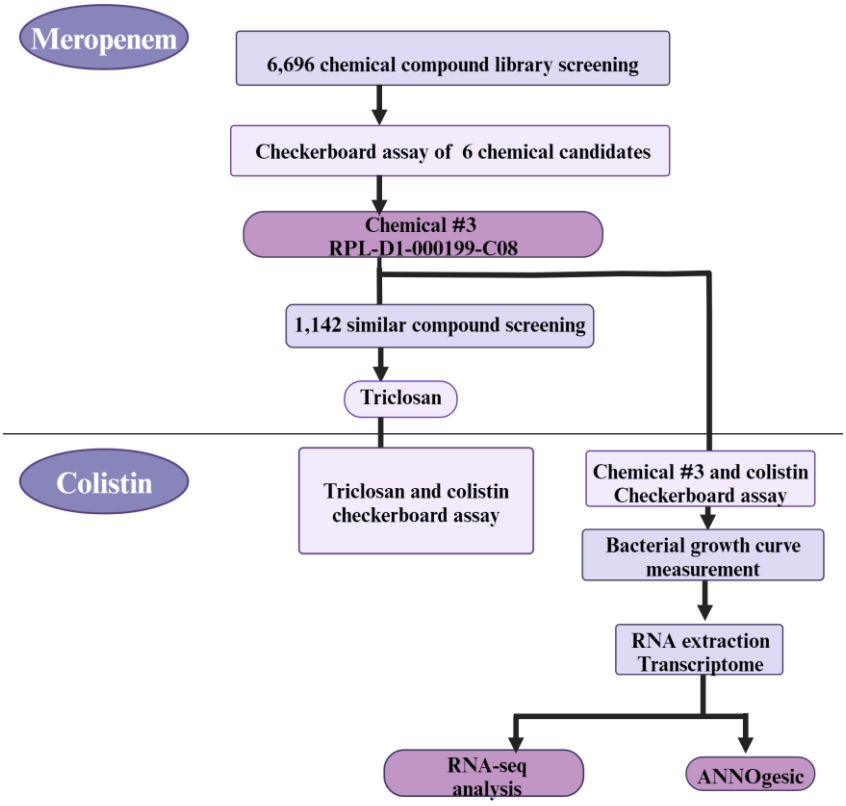

Figure 4. An overview of phenotypic and genotypic approaches.

2.2.2. Checkerboard analysis

A single colony of the strain was selected and adjusted to a 0.5 McFarland standard. Before inoculation, it was diluted (1:100) in cation-adjusted Mueller-Hinton broth. Serial dilutions were performed for meropenem (Yuhan, Seoul, South Korea), colistin (Sigma-Aldrich, St. Louis, MO, USA), chemical #3 (LegoChem Biosciences, Daejeon, South Korea), and triclosan (Sigma-Aldrich, St. Louis, MO, USA). The definition of MIC was the lowest concentration without observable growth. The fractional inhibitory concentration index (FICI) was derived with the formula: FICI = FICA + FICB = MICAB / MICA + MICBA / MICB. Here, MICAB represents compound A's MIC in conjunction with compound B, MICA represents compound A's concentration alone, MICBA represents compound B's concentration with compound A, and MICB represents compound B's MIC alone. The FICI range for interpretation was as follows: FICI $\leq$ 0.5 suggested synergy, 0.5 < FICI $\leq$ 1 showed additive effect, 1 < FICI $\leq$ 2 indicated no interaction, and FICI > 2 indicated antagonism (Table 2)

2.2.3. Bacterial growth curve assessment

Growth curves were measured using a 96-well clear, flat-bottom microplate (SPL Life Sciences, Kyeonggido, South Korea) and optical adhesive films (Thermo Fisher Scientific, Waltham, MA, USA) in a microplate reader (Molecular Devices, San Jose, CA, USA). The microplate reader was programmed to make optical density measurement at 600 nm every 10 minutes for 24 hours. The midway of the logarithmic phase of bacterial development was identified. the standard deviation marked with error bars. GraphPad Prism v9.3.0 was used for statistical analysis, namely the Student's t-test (Figure 5).

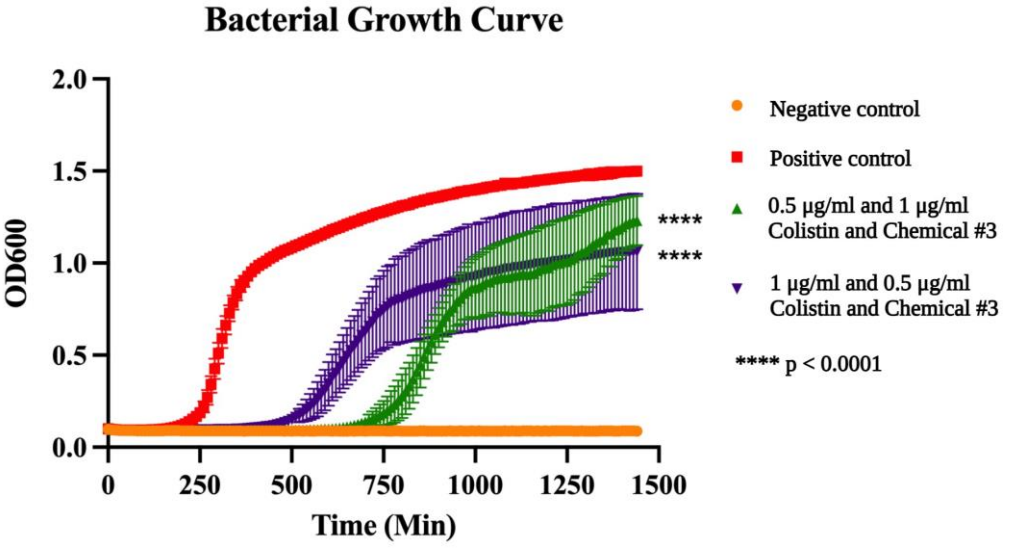

Figure 5. Bacterial growth curve to determine the mid-log phase.

2.2.4. RNA Extraction

The treatment consisted of 0.5 μg/ml colistin and 1 μg/ml chemical #3 diluted with Luria broth in round-bottom tubes. After 14 hours and 50 minutes of incubation, cells were collected and RNA was extracted with the RNeasy mini kit and RNase-free DNase set (Qiagen, Hilden, Germany) as per manufacturer's instructions. RNA quality was measured with a NanoDrop spectrophotometer (Thermo Fisher Scientific, Waltham, MA, USA).

2.2.5. Transcriptome analysis

The Illumina total RNA-seq assay utilized a stranded total RNA library prep kit. The Yonsei University Genome Center used the Nextseq550 sequencing platform to sequence libraries. The Bioinformatics Collaboration Unit at Yonsei University College of Medicine evaluated the RNA-seq data. During processing and quality control, bcl format files were converted to fastq files with bcl2fastq2 (v2.20.0.422). Adapter and quality trimming were done with Cutadapt (v1.18)[23] and Trimmomatic (v0.32)[24]. Before and after trimming, quality checks were performed using FastQC (v0.11.7)[25]. The reference genome of Klebsiella pneumoniae HS strain 11286 was aligned and transcriptome assembled using HISAT2 (v2.1.0)[26] and StringTie (v2.0.6)[27]. The LPEseq[28] statistical technique was used to do differential expression analysis. Normalized count values, p-values, and q-values were reported without replications.

2.2.6. Data processing and analysis

The READemption program (v2.0.3)[29] generated a coverage wiggling file from the fastq files of the complete RNA-seq dataset. The ANNOgesic tool (v1.1.14)[8] was used to identify subcommand sRNA and its targets through RNAplex. We used the Rfam and Infernal databases (https://github.com/Sung-Huan/ANNOgesic) to predict riboswitches and RNA thermometers. KlebNet[2] and Cytoscape (version 3.9.1)[30] were used for network-based functional analysis. Perseus[31] was used to create clustering heatmaps and visualize pathways. The Venn diagrams figures were formed using VENNY (2.1.0)[32].

2.2.7. Transmission Electron Microscope (TEM) analysis

The Yonsei University Electron Microscopy Center's TEM analysis involves five steps: constructing blocks, creating semithin slides, arranging them on grids, negative staining, and imaging. Following fixation and washing, the specimens were embedded. Then, 200nm thick slide pieces were generated. Interested regions were cut into 80nm slices with an ultramicrotome. Ultra-thin portions were put in copper grids. Negative staining was used to study the structure and size of bacteria. The photos were taken with JEM-1011 (JEOL, Tokyo, Japan) and Camera-Megaview III (Soft Imaging System-Germany, Münster, Germany).

2.3. Experimental approaches to validate transcriptome analysis

2.3.1. Reverse Transcription Polymerase Chain Reaction (RT-PCR)

cDNA was synthesized with TaqMan Reverse Transcription Reagent Kit (ThermoFisher Scientific, Waltham, MA, USA) and PCR machine T100 Thermal Cycler (Bio-Rad, Hercules, CA, USA).

2.3.2. TaqMan probe and primer design

The primer was designed with a GeneScript primer design tool (GeneScript Biotech, Piscataway, NJ, USA).

2.3.3. Real-Time quantitative Polymerase Chain Reaction (qPCR)

QuantSutdio Real-Time PCR Systems (ThermoFisher Scientific, Waltham, MA, USA) detected changes in gene expression, and TaqMan Fast Advanced Master Mix (ThermoFisher Scientific, Waltham, MA, USA) was utilized as a real-time PCR kit.

2.3.4. Adenosine triphosphate (ATP) measurement

Bac Titer-Glo Microbial Cell Viability Assay (Promega, Madison, WI, USA) was used to determine ATP related to cell number. Luminescence was measured with a Centro XS3 LB960 (Berthold Technology, Baden Wurttemberg, Germany).

2.3.5. Statistical analysis

Nonparametric one-way ANOVA statistical analysis with the Friedman test was performed with GraphPad Prism (version 9.3.0)

2.4. Two-dimensional (2DE) gel electrophoresis-based proteome analysis at the protein level

The samples were prepared in four conditions (K56, K56_Colistin, K56_Chemical#3, and K56_Colistin_Chemical#3) for 2DE images and Liquid Chromatography-Mass Spectrometry (LC-MS/MS) of peptide analysis. The following procedures were processed at the Yonsei Proteome Research Center. 2DE gel electrophoresis and staining were performed[33]. From cutting protein spots and stain removal to peptide extraction via in-gel tryptic digestion[34] steps were carried out. Ultimately, LC-MS/MS analysis with database searching[35] was applied with the taxonomy *Klebsiella pneumoniae subsp. pneumoniae* HS11286 from NCBI.

2.5. Cheminformatic on the genomic level

2.5.1. Pangenome analysis for target identification

Prokka[36] annotated the bacterial sequence from the genome to generate the input file for Roary (https://vicbioinformatics.com) algorithms, which then evaluated the pangenome[37] (https://sanger-pathogens.github.io/Roary). Two-nucleotide sequences were aligned utilizing BLASTN (Nucleotide Basic Local Alignment Search Tool) (https://www.blast.ncbi.nlm.nih.gov/doc/blast-

help/downloadblastdata.html) to identify target genes. A STRING protein-protein interaction network (https://string-db.org) and cytoscape (https://cytoscape.org) were used to visualize complex networks.

2.5.2. Protein model generation and evaluation for docking

2.5.2.1. Homology modeling and scoring

From NCBI (National Center for Biotechnology Information) (https://www.ncbi.nlm.nih.gov), maltoporin's amino acid sequence (KPHS_02600) was downloaded in FASTA format. HOMELETTE, along with integrated modeling software (https://github.com/PhilippJunk/homelette/), projected the target protein structure during the template identification, alignment generation, model generation, and model evaluation processes[38].

2.5.2.2. Physiochemical parameter computation

The ProtParam tool on the Expasy server (https://web.expasy.org) analyzes the physicochemical characteristics of proteins based on their input sequence. The following values were resolved: number of amino acids, molecular weight, theoretical pI, amino acid composition, atomic composition, extinction coefficient, estimated half-life, instability index, aliphatic index, and grand average of hydropathicity (GRAVY).

2.5.2.3. Proteins and ligand preparation for molecular docking

Proteins were prepared using AutoDock Vina's multiple ligand docking section guidelines[39,40]. Openbabel[41] was used to transform colistin's sdf into pdbqt format. Ligand preparation was completed in AutoDock Vina.

2.5.2.4. Protein and multiple ligand docking

PrankWeb was used to determine active sites. It depicted ligand binding locations and applied machine learning[42] (https://prankweb.cz) to establish x, y, and z coordinates. The active docking site for the homologically modeled protein structure is (X:0.691; Y:52.0375; Z:66.8974). Meropenem and other chemical compounds were docked into a predicted protein model. Additionally, the combined docking activity of chemical #3 and colistin was generated in AutoDock Vina, demonstrating simultaneous docking of multiple ligands[39,40]. PyMOL was used to produce complex models and view them in three dimensions (https://www.pymol.org/2/). LigPlotPlus (v.2.2.8) visualized interactions between ligands and protein using 2-dimensional structural information[43].

2.5.2.5. Physiological features and similarities comparison

ADMETlab (https://admetmesh.scbdd.com) was used to assess the ligand characteristics[44]. The Tanimoto coefficient[45] was calculated as part of a ligand similarity analysis using the ChemMine Tool (https://chemminetools.ucr.edu).

2.5.2.6. Molecular dynamics simulation

With the selected 7 different multiple ligands, the NAMD (Nanoscale Molecular Dynamics) software ran 10 ns (nanoseconds) simulations (https://www.ks.uiuc.edu/Research/namd/). The PDB reader and solution builder of MolCube produced inputs for the simulation (https://www.molcube.xyz/). A CHARMM 36m forcefield was used. A cube solvation box with 0.15 M KCl neutralized the system. The temperature was set at 303.15 K. MD ran using 100 frames with a 4 fs time step. Visual Molecular Dynamics (VMD) performed post MD analysis including root mean secure deviation (RMSD), root mean square fluctuation (RMSF), intramolecular hydrogen bonding, radius of gyration (Rg), and solvent accessible surface area (SASA) (https://www.ks.uiuc.edu/Research/vmd/).

3. Results

A checkerboard experiment was used to determine phenotypic susceptibility. Colistin, chemical #3, and triclosan MIC values of K56 were 64, 16, and 4 μg/ml, respectively. Combining 0.5 μg/ml colistin with 2 μg/ml chemical #3 and 1 μg/ml colistin with 1 μg/ml chemical #3 yielded fractional inhibitory concentration index values significantly lower than 0.5, indicating a strong interaction. Both colistin and triclosan had synergistic effects in the testing results. However, because chemical #3 is similar to triclosan, which has known negative effects and toxicity, it should be approached with caution as a potential medicinal component (Table 2).

Table 2. Checkerboard assay for phenotypic susceptibility

Antimicrobial combination (MIC, μg/mL)				
Characteristics	**Colistin + Che #3**	**Colistin + Che #3**	**Colistin + Triclosan**	**Colistin + Triclosan**
	0.5 + 2	1 + 1	0.5 + 1	1 + 0.5
FICindex	0.133	0.078	0.258	0.141
Potentiation (fold)	128	64	128	64
Interpretation	Synergy	Synergy	Synergy	Synergy

3.1. Resistant genes and pathogenesis

In Figure 6, pangenome was demonstrated with a Bandage tool. The edges indicate connections between nodes, contained in assembly graphs[21]. For confirmation purposes, the circular genome graph to view the genotypic difference between K26 and K56 was created with BRIG[22]. As demonstrated in Figure 7, these two strains are very similar but not identical. There are missing areas in the visualized genomic ranges.

The genome comparison represents less alteration between the K26 and K56 (Table 3). The resistance genes are the same except for the type of beta-lactamase genes, K26 with blaSHV-12 and K56 with blaSHV-187. However, the blaSHV-187 has the %coverage and %identity values 81.31 and 99.57. It is not 100%.

The virulence factors are in the same situation as antimicrobial resistance (AMR) genes.The virulence factors of K26 and K56 strains were in various classes such as adherence, antiphagocytosis, efflux pump, iron uptake, regulation, secretion system, and toxin. K56 has the same virulence factors as K26 although there is a genomic evolutionary alternation in pangenome analysis (Table 4).

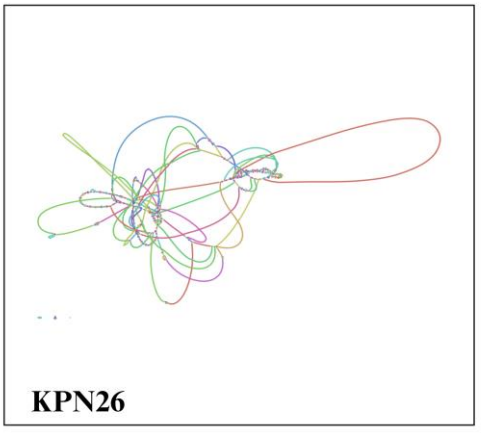

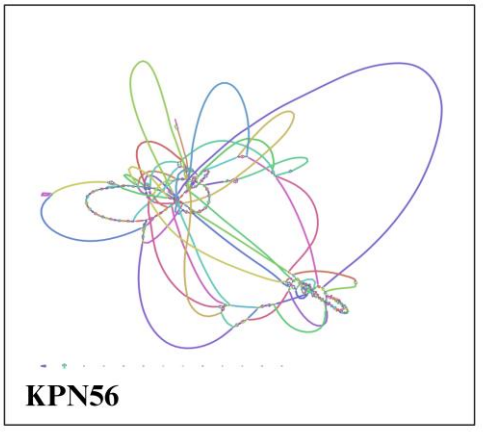

Figure 6. Visualization of pangenome with contigs (nodes) and connections (edges).

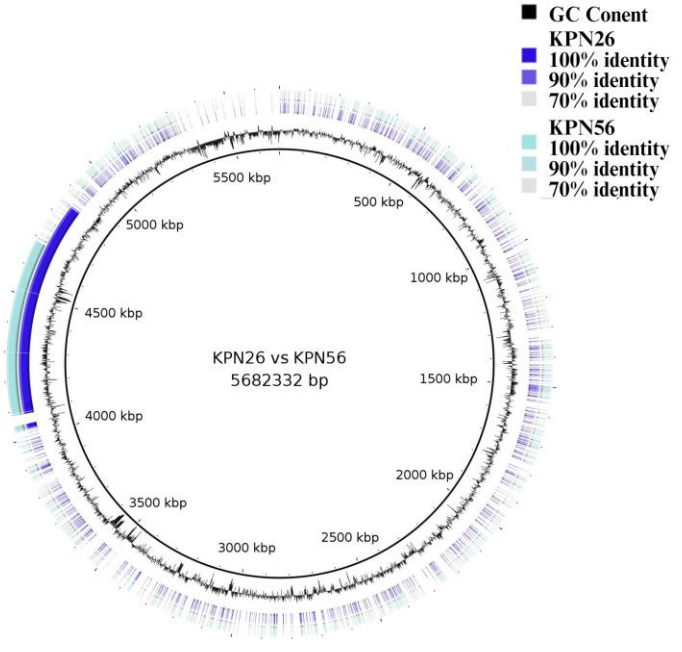

Figure 7. Genomic comparison between K26 and K56.

Table 3. Antimicrobial resistant (AMR) gene of K26 vs K56 with NCBI database from ABRicate

Strain	SEQUENCE	START	END	STRAND	GENE	COVERAGE	GAPS	%COVERAGE	%IDENTITY	ACCESSION	PRODUCT	RESISTANCE
K26	NODE_15_length_124348_cov_10.617520	109853	110272	-	*fosA6*	1-420/420	0/0	100	98.81	NG_051497.1	fosfomycin resistance glutathione transferase FosA6	FOSFOMYCIN
	NODE_1_length_803287_cov_11.193605	768141	771293	-	*oqxB*	1-3153/3153	0/0	100	100	NG_048025.1	multidrug efflux RND transporter permease subunit OqxB	PHENICOL;QUINOLONE
	NODE_1_length_803287_cov_11.193605	771317	772492	-	*oqxA*	1-1176/1176	0/0	100	100	NG_048024.1	multidrug efflux RND transporter periplasmic adaptor subunit OqxA	PHENICOL;QUINOLONE
	NODE_42_length_10811_cov_6.256926	1849	2733	-	*mph(E)*	1-885/885	0/0	100	100	NG_064660.1	Mph(E) family macrolide 2'-phosphotransferase	MACROLIDE
	NODE_42_length_10811_cov_6.256926	2789	4264	-	*msr(E)*	1-1476/1476	0/0	100	100	NG_048007.1	ABC-F type ribosomal protection protein Msr(E)	MACROLIDE
	NODE_42_length_10811_cov_6.256926	6563	7336	-	*armA*	1-774/774	0/0	100	100	NG_047476.1	ArmA family 16S rRNA (guanine(1405)-N(7))-methyltransferase	GENTAMICIN
	NODE_45_length_6726_cov_5.405213	4099	4935	-	*aph(6)-Id*	1-837/837	0/0	100	100	NG_047464.1	aminoglycoside O-phosphotransferase APH(6)-Id	STREPTOMYCIN
	NODE_45_length_6726_cov_5.405213	4935	5762	-	*aph(3'')-Ib*	1-828/828	0/0	100	99.88	NG_056002.2	aminoglycoside O-phosphotransferase APH(3'')-Ib	STREPTOMYCIN
	NODE_50_length_3781_cov_7.319923	1434	2573	+	*bla*DHA-1	1-1140/1140	0/0	100	100	NG_049055.1	class C beta-lactamase DHA-1	CEPHALOSPORIN
	NODE_51_length_3320_cov_71.600689	24	884	+	*bla*SHV-12	1-861/861	0/0	100	100	NG_050590.1	class A extended-spectrum beta-lactamase SHV-12	CEPHALOSPORIN
	NODE_52_length_3063_cov_14.640327	1954	2793	-	*sul1*	1-840/840	0/0	100	100	NG_048082.1	sulfonamide-resistant dihydropteroate synthase Sul1	SULFONAMIDE
	NODE_57_length_2222_cov_9.605251	362	1153	-	**aadA2**	1-792/792	0/0	100	100	NG_051846.1	ANT(3'')-Ia family aminoglycoside nucleotidyltransferase AadA2	STREPTOMYCIN
K56	NODE_16_length_124455_cov_28.116860	14077	14496	+	*fosA6*	1-420/420	0/0	100	98.81	NG_051497.1	fosfomycin resistance glutathione transferase FosA6	FOSFOMYCIN
	NODE_1_length_644183_cov_29.464017	30796	31971	+	*oqxA*	1-1176/1176	0/0	100	100	NG_048024.1	multidrug efflux RND transporter periplasmic adaptor subunit OqxA	PHENICOL;QUINOLONE
	NODE_1_length_644183_cov_29.464017	31995	35147	+	*oqxB*	1-3153/3153	0/0	100	100	NG_048025.1	multidrug efflux RND transporter permease subunit OqxB	PHENICOL;QUINOLONE
	NODE_40_length_10812_cov_10.040618	1850	2734	-	*mph(E)*	1-885/885	0/0	100	100	NG_064660.1	Mph(E) family macrolide 2'-phosphotransferase	MACROLIDE
	NODE_40_length_10812_cov_10.040618	2790	4265	-	*msr(E)*	1-1476/1476	0/0	100	100	NG_048007.1	ABC-F type ribosomal protection protein Msr(E)	MACROLIDE
	NODE_40_length_10812_cov_10.040618	6564	7337	-	*armA*	1-774/774	0/0	100	100	NG_047476.1	ArmA family 16S rRNA (guanine(1405)-N(7))-methyltransferase	GENTAMICIN
	NODE_44_length_6725_cov_8.216884	4099	4935	-	*aph(6)-Id*	1-837/837	0/0	100	100	NG_047464.1	aminoglycoside O-phosphotransferase APH(6)-Id	STREPTOMYCIN
	NODE_44_length_6725_cov_8.216884	4935	5762	-	*aph(3'')-Ib*	1-828/828	0/0	100	99.88	NG_056002.2	aminoglycoside O-phosphotransferase APH(3'')-Ib	STREPTOMYCIN
	NODE_49_length_3781_cov_8.855227	1434	2573	+	*bla*DHA-1	1-1140/1140	0/0	100	100	NG_049055.1	class C beta-lactamase DHA-1	CEPHALOSPORIN
	NODE_50_length_3063_cov_31.185286	1954	2793	-	*sul1*	1-840/840	0/0	100	100	NG_048082.1	sulfonamide-resistant dihydropteroate synthase Sul1	SULFONAMIDE
	NODE_54_length_2222_cov_35.268258	1070	1861	+	*aadA2*	1-792/792	0/0	100	100	NG_051846.1	ANT(3'')-Ia family aminoglycoside nucleotidyltransferase AadA2	STREPTOMYCIN
	NODE_77_length_722_cov_75.137815	1	705	-	*bla*SHV-187	1-705/867	0/0	81.31	99.57	NG_050053.1	class A beta-lactamase SHV-187	BETA-LACTAM

Table 4. Virulence factors of K26 and K56 based on Virulence Factor Database

VF class	Virulence factors	Related genes	KPN26(Prediction)	K.pneumoniae subsp. pneumoniae HS11286	KPN56(Prediction)
Adherence	Type 3 fimbriae	*mrkA*	orf00472	KPHS_43470	orf00337
		mrkB	orf00473	KPHS_43460	orf00336
		mrkC	orf00474	KPHS_43450	orf00335
		mrkD	orf00475	KPHS_43440	orf00334
		mrkF	orf00476	KPHS_43430	orf00333
		mrkH	orf00479	KPHS_43400	orf00330
		mrkI	orf00478	KPHS_43410	orf00331
		mrkJ	orf00477	KPHS_43420	orf00332
	Type I fimbriae	*fimA*	orf00463	KPHS_43550	orf00346
		fimB	orf00467	KPHS_43520	orf00342
		fimC	orf00461	KPHS_43570	orf00348
		fimD	orf00460	KPHS_43580	orf00349
		fimE	orf00465	KPHS_43530	orf00344
		fimF	orf00459	KPHS_43590	orf00350
		fimG	orf00458	KPHS_43600	orf00351
		fimH	orf00457	KPHS_43610	orf00352
		fimI	orf00462	KPHS_43560	orf00347
		fimK	orf00456	KPHS_43620	orf00353
Antiphagocytosis	Capsule	-	orf03981; orf03982; orf03989; orf03990; orf03991; orf03992; orf03993; orf03994; orf04470	KPHS_35540; KPHS_35550; KPHS_35560; KPHS_35570; KPHS_35580; KPHS_35590; KPHS_35600; KPHS_35610; KPHS_35620; KPHS_35630; KPHS_35640; KPHS_35650; KPHS_35660; KPHS_35670; KPHS_35680; KPHS_35690; KPHS_35700; KPHS_35730; KPHS_35740	orf04003; orf04004; orf04010; orf04011; orf04012; orf04013; orf04014; orf04015; orf04387
Efflux pump	AcrAB	*acrA*	orf01960	KPHS_11890	orf01890
		acrB	orf00002; orf01961	KPHS_11880	orf01891; orf03333

Table 4. Virulence factors of K26 and K56 based on Virulence Factor Database

VF class	Virulence factors	Related genes	KPN26(Prediction)	K.pneumoniae subsp. pneumoniae HS11286	KPN56(Prediction)
Iron uptake	Aerobactin	*iucA*	-	-	-
		iucB	-	-	-
		iucC	-	-	-
		iucD	-	-	-
		iutA	orf00880	KPHS_19870	orf01080
	Ent siderophore	*entA*	orf04303	KPHS_14490	orf04236
		entB	orf04304	KPHS_14480	orf04235
		entC	orf04306	KPHS_14460	orf04233
		entD	orf04316	KPHS_14360	orf04223
		entE	orf04305	KPHS_14470	orf04234
		entF	orf04312	KPHS_14400	orf04227
		entS	orf04308	KPHS_14440	orf04231
		fepA	orf04315; orf04611	KPHS_14370	orf04224; orf04526
		fepB	orf04307	KPHS_14450	orf04232
		fepC	orf04311	KPHS_14410	orf04228
		fepD	orf04309	KPHS_14430	orf04230
		fepG	orf04310	KPHS_14420	orf04229
		fes	orf04314	KPHS_14380	orf04225
	Salmochelin	*IroB*	-	-	-
		iroC	-	-	-
		iroD	-	-	-
		iroE	orf01480	KPHS_26150	orf01232
		iroN	orf04600	KPHS_21440	orf04515
	Yersiniabactin	*fyuA*	orf02428	KPHS_34710	orf02146
		irp1	orf02424	KPHS_34670	orf02150
		irp2	orf02423	KPHS_34660	orf02151
		ybtA	orf02422	KPHS_34650	orf02152
		ybtE	orf02427	KPHS_34700	orf02147
		ybtP	orf02421	KPHS_34640	orf02153
		ybtQ	orf02420	KPHS_34630	orf02154
		ybtS	orf02418	KPHS_34610	orf02156
		ybtT	orf02426	KPHS_34690	orf02148
		ybtU	orf02425	KPHS_34680	orf02149
		ybtX	orf02419	KPHS_34620	orf02155
	Ferrous iron transport(Shigella)	*sitC*	orf02403	-	orf02171
	Iron/manganese transport(Escherichia)	*sitD*	orf02404	-	orf02170
Nutritional factor	Allantoin utilization	*allA*	-	-	-
		allB	-	-	-
		allC	-	-	-
		allD	-	-	-
		allR	-	-	-
		allS	-	-	-
Regulation	RcsAB	*rcsA*	orf02364	KPHS_34420	orf02208
		rcsB	orf02885	KPHS_37040	orf03871
	RmpA	*rmpA*	-	-	-

Table 4. Virulence factors of K26 and K56 based on Virulence Factor Database

VF class	Virulence factors	Related genes	KPN26(Prediction)	K.pneumoniae subsp. pneumoniae HS11286	KPN56(Prediction)
Secretion system	T6SS-I	-	orf03012	KPHS_23050	orf03162
		-	orf03018	KPHS_23120	orf03155
		-	orf03019	KPHS_23130	orf03154
		clpV/tssH	orf03010	KPHS_23030	orf03164
		dotU/tssL	orf03007	KPHS_23000	orf03167
		hcp/tssD	orf03009	KPHS_23020	orf03165
		icmF/tssM	orf03020	KPHS_23140	orf03153
		impA/tssA	orf03021	KPHS_23150	orf03152
		ompA	orf03008	KPHS_23010	orf03166
		sciN/tssJ	orf03025	KPHS_23190	orf03148
		tle1	-	KPHS_23105	-
		tli1	orf03013; orf03014; orf03015; orf03016	KPHS_23060; KPHS_23070; KPHS_23080; KPHS_23090	orf03157; orf03158; orf03159; orf03160; orf03161
		tssF	orf03023	KPHS_23170	orf03150
		tssG	orf03024	KPHS_23180	orf03149
		vasE/tssK	orf03006	KPHS_22990	orf03168
		vgrG/tssI	orf03011	KPHS_23040	orf03163
		vipA/tssB	orf03004	KPHS_22970	orf03170
		vipB/tssC	orf03005	KPHS_22980	orf03169
	T6SS-II	*clpV*	orf00810	KPHS_39850	orf00001
		dotU	-	-	-
		icmF	-	-	-
		impF	-	-	-
		impH	-	-	-
		impJ	-	-	-
		ompA	-	-	-
		sciN	-	-	-
		vasA/impG	-	-	-
		vgrG	-	-	-
	T6SS-III	-	-	KPHS_32780	-
		-	orf04950	KPHS_32740	orf04964
		-	-	-	-
		-	-	-	-
		-	-	-	-
		-	orf01890	KPHS_32440	orf01515
		-	orf01889	KPHS_32430	orf01516
		dotU	orf04948	KPHS_32760	orf04962
		icmF	orf01896	KPHS_32500	orf01509
		impA	orf01891	KPHS_32450	orf01514
		impF	orf01892	KPHS_32460	orf01513
		impG	orf01895	KPHS_32490	orf01510
		impH	orf01894	KPHS_32480	orf01511
		impJ	orf04947	KPHS_32770	orf04961
		lysM	-	-	-
		ompA	orf04949	KPHS_32750	orf04963
		sciN	orf01893	KPHS_32470	orf01512
		vgrG	orf04951	KPHS_32730	orf04965
Serum resistance	LPS rfb locus	-	-	KPHS_35440; KPHS_35450; KPHS_35460; KPHS_35470; KPHS_35480; KPHS_35490; KPHS_35500	-
Toxin	Colibactin	*clbA*	-	-	-
		clbB	orf04976	-	orf04890
		clbC	orf04977	-	orf04891
		clbD	-	-	-
		clbE	-	-	-
		clbF	orf04980	-	orf04894
		clbG	orf04981	-	orf04895
		clbH	orf04982	-	orf04896
		clbI	orf04983	-	orf04897
		clbJ	-	-	-
		clbK	-	-	-
		clbL	orf02451	-	orf02125
		clbM	orf02450	-	orf02126
		clbN	orf02449	-	orf02127
		clbO	orf02448	-	orf02128
		clbP	orf02447	-	orf02129
		clbQ	orf02446	-	orf02130
		clbS	-	-	-

3.2. Interactions of K56 and the single treatment with chemical #3

3.2.1. K56 mode of action under chemical #3 only treatment

Six compounds from the 6,696 chemical library obtained synergistic reactions with meropenem. However, at low concentrations, only the chemical #3 treatment remained an additive. In the following stage, meropenem was substituted with colistin, which subsequently functioned in conjunction with chemical #3. According to the Pearson correlation coefficient value (0.996), chemical #3 alone had substantial similarity in gene expression with the control group (Figure 8C). The single treatment also had much fewer differentially expressed genes (DEGs) than the combination treatment (Figure 8E).

Inositol catabolism is a metabolic process that happens during chemical #3 treatment. Inositol plays a role in phospholipid cell membranes[46]. In BiCU's Figure 9, the downregulated inositol-1,2,3,4,5 phosphates are shown, although myo-inositol gene expression remains unchanged. Conversely, reduced D-chiro-inositols lead to lower carbon availability under nutrient-poor conditions, but there are still no cell permeability alterations through phospholipid. Bacteria work for transport as well as phosphorylation in the sugar phosphotransferase system (PTS)[47]. The downregulated phosphoenolpyruvate-dependent PTS family enzymes IIA component, KPHS_26190 (MtlA), is involved in the phosphorylation cascade (Figure 10 from BiCU). Hence, energy

levels are lowered as a consequence of reduced sugar transport and phosphorylation.

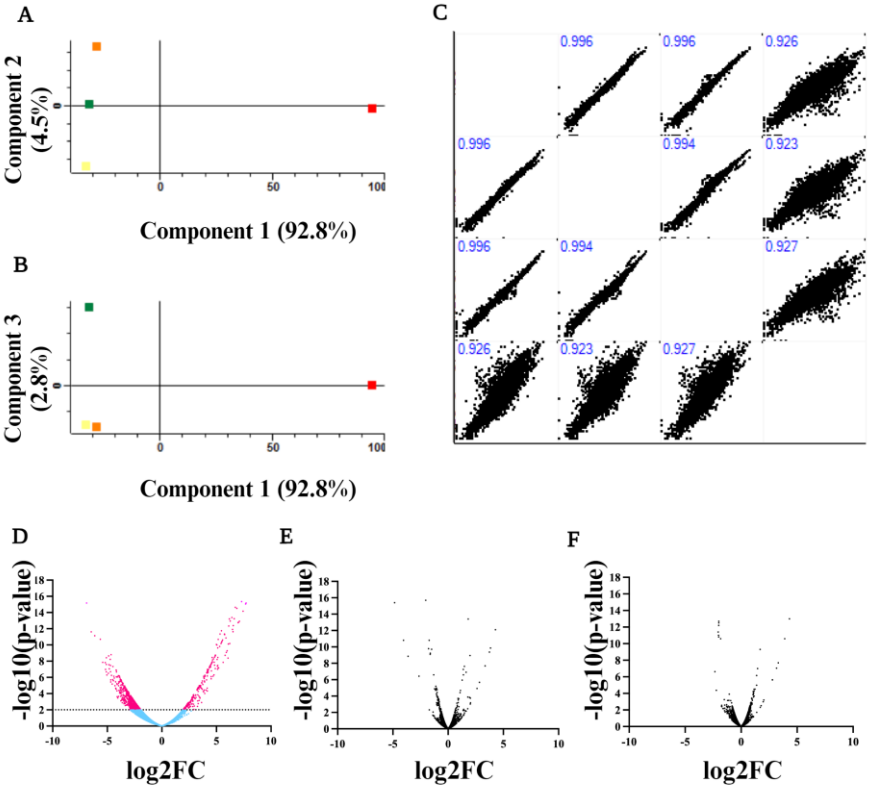

Figure 8. Transcriptome analysis plots. Colistin and chemical #3 combination therapy indicated differently in overall graphs. The combination treatment (red), chemical #3 single treatment (orange), colistin single treatment (yellow), and control (green) groups are displayed. (A) and (B) are principal component analysis

for components 1 and 2 and components 1 and 3, respectively. The graphs have a higher significance for the combined one. Panel (C) demonstrates multiple scatter plots, demonstrating a positive connection in the linear relationship of the correlated data. This distribution exposes patterns and correlations. The combination had a wider numerical spread (correlation coefficients) than the two individual treatments and the control. They are between 0.923 and 0.996. Higher values are interpreted as adjacent linear correlations. Volcano plots are (D) control vs. combination treatment, (E) control vs. chemical #3 treatment, and (F) control vs. colistin treatment groups. The log2 fold change (log2FC) is denoted by the x-axis. The LPEseq technique calculated -log10 (p-value) for the y-axis. The left side exhibits gene down regulation. The right side of the plot displays an upregulation. For identifying DEGs, the cutoff at a p-value equal to 0.01 is marked with a dotted line. Non-DEGs and DEGs are represented by blue and pink dots. (D) The combination treatment demonstrates a much higher number of expressed genes when compared to single treatment plots (E) and (F).

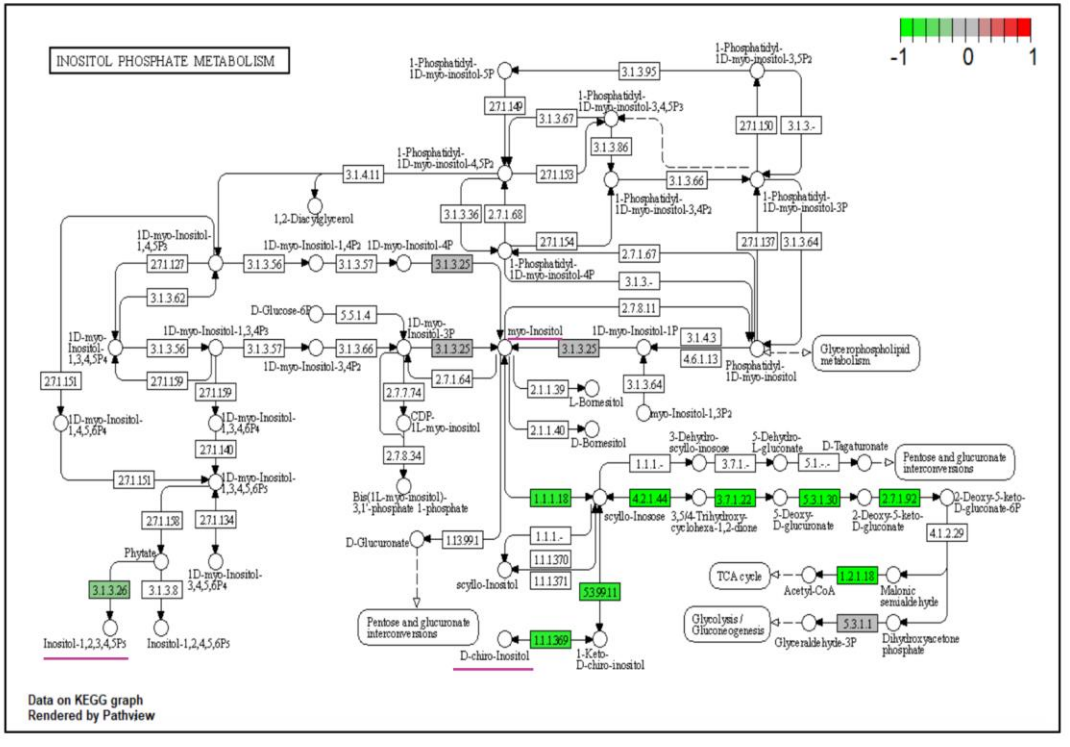

Figure 9. Inositol phosphate metabolism of chemical #3 in a single treatment. Green rectangles show that associated genes are downregulated. Gray represents no change in gene expression.

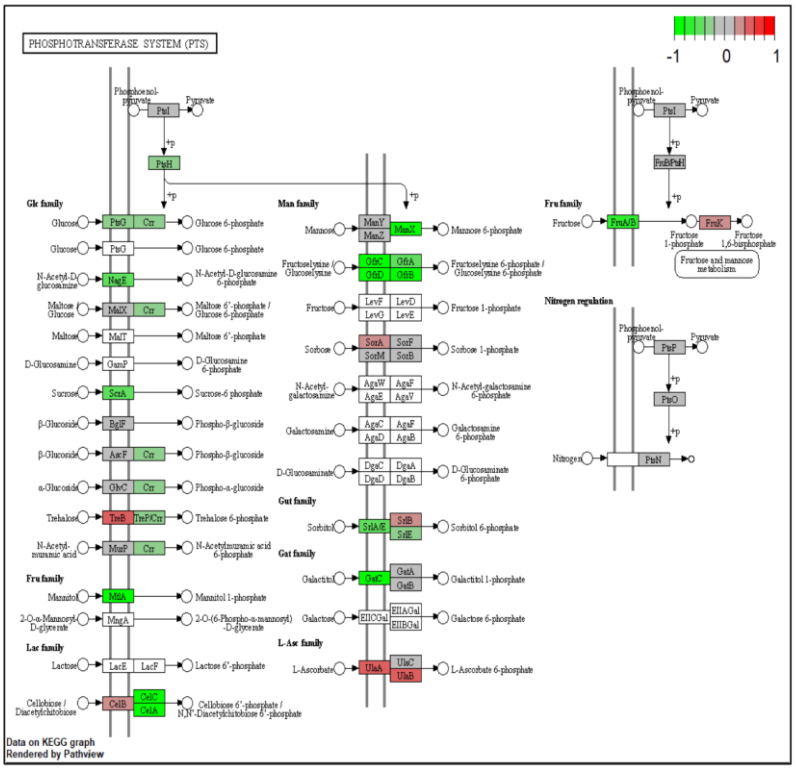

Figure 10. Phosphotransferase system for chemical #3 in a single treatment. The map depicts reaction steps involving different molecules. Red signifies that gene expression is increased.

3.2.2. Gene expression of combo colistin and chemical #3 against K56

The combination treatment had a more significant effect on gene expression than in the single treatment groups and the control group (Figures 8, 11, and 12), validated by correlation analysis (Figure 8). To find affecting factors, a differential expression analysis was performed with volcano graphs and identified 580 downregulation and 242 upregulation genes. There were no central overlaps across all the three different groups (Figure 13).

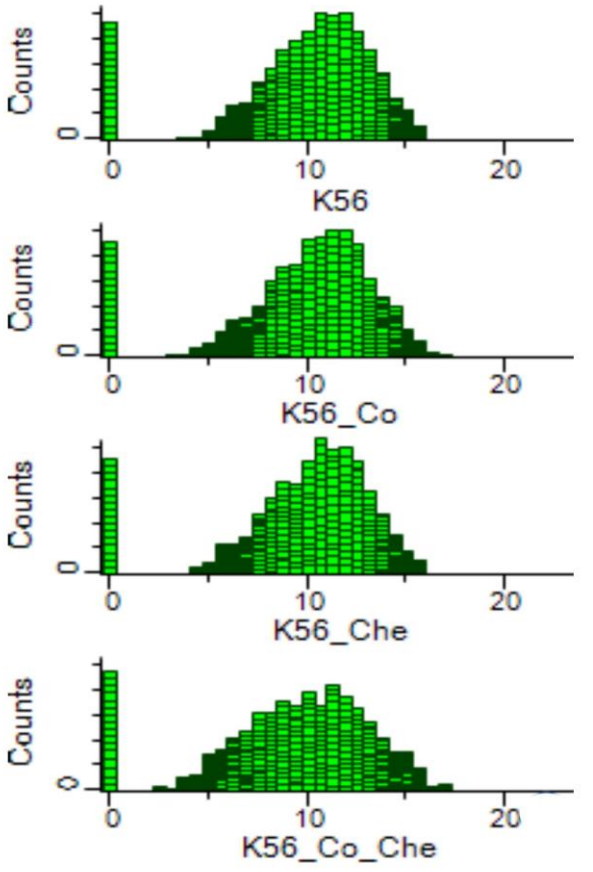

Figure 11. Histograms of gene distribution. Histograms reflect gene counts vs. numerical values and are used to evaluate multiple scatter plots.

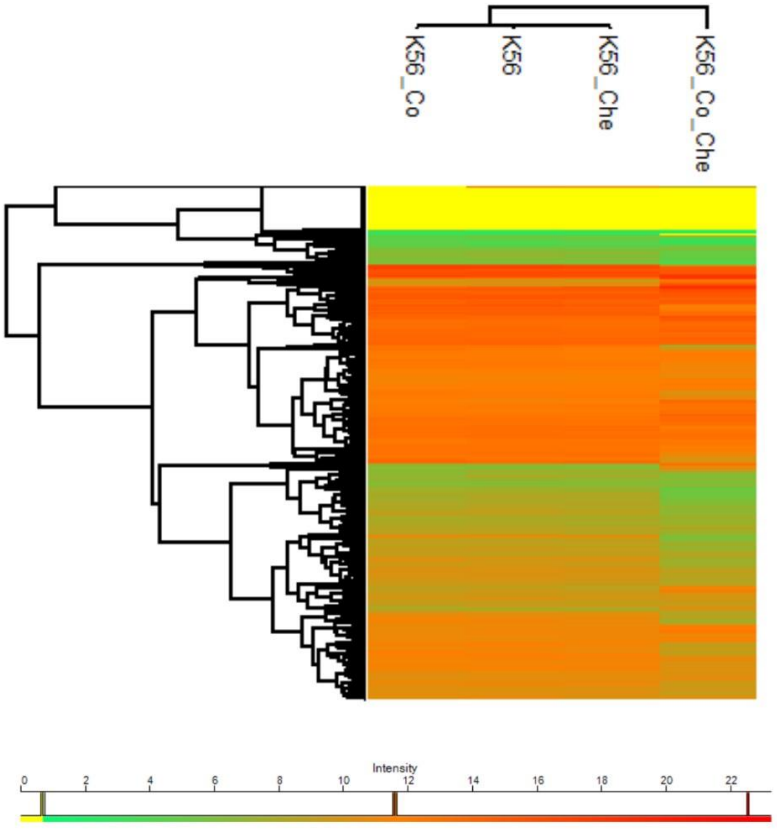

Figure 12. Hierarchical clustering and heatmap. Clustering analysis showed that the control group (K56) and two single-treatment groups had similar patterns, but the combination treatment with colistin and chemical #3 differed.

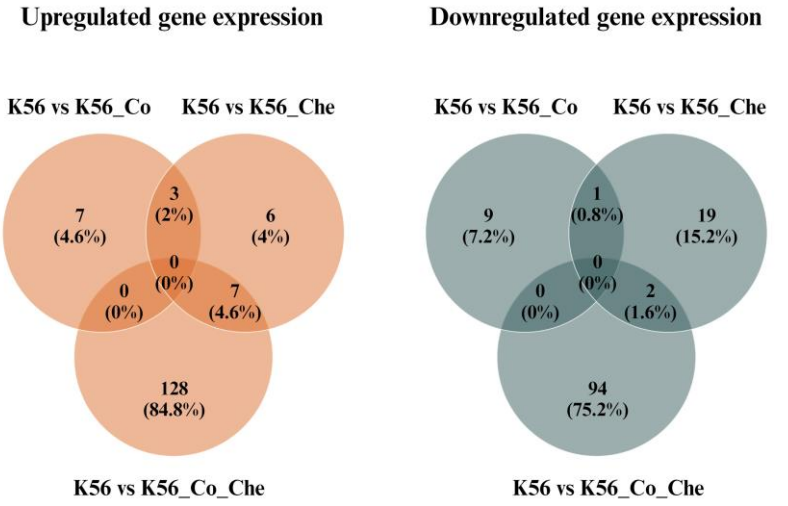

Figure 13. Venn diagrams. (A) displays upregulated genes, whereas (B) represents downregulated genes. The left, right, and bottom circles in (A) represent 7, 6, and 128 genes with enhanced expression, respectively. Genes in (B), 9, 19, and 94 showed reduced expression. The exclusive areas at the bottom of both panels were implicated in a variety of pathways associated with the combo treatment's mode of action. The core common area contained no overlapping genes in terms of expression, indicating that the three treatments had no shared features.

3.2.3. Phenylalanine metabolism with general downregulation

Lower levels of succinyl-CoA and acetyl-CoA are occurred by reduced phenylacetate-CoA oxygenase subunit PaaA (KPHS_23690) and phenylacetic acid degradation protein (KPHS_23710) (Figure 14A)[48]. It has a deleterious impact on the citrate cycle. These genes were negatively connected to bacterioferritin (KPHS_48720). After exposure to the combination, the iron transport system correlates with the porphyrin metabolism pathway (Figure 15A). Table 5 exhibits that the attenuator RNA thermometer associated with 6-phosphofructokinase (KPHS_31750) (https://rfam.org). In the gene network (Figure 15A), the gene is linked as a potential contributor to the negative gene expression tendency.

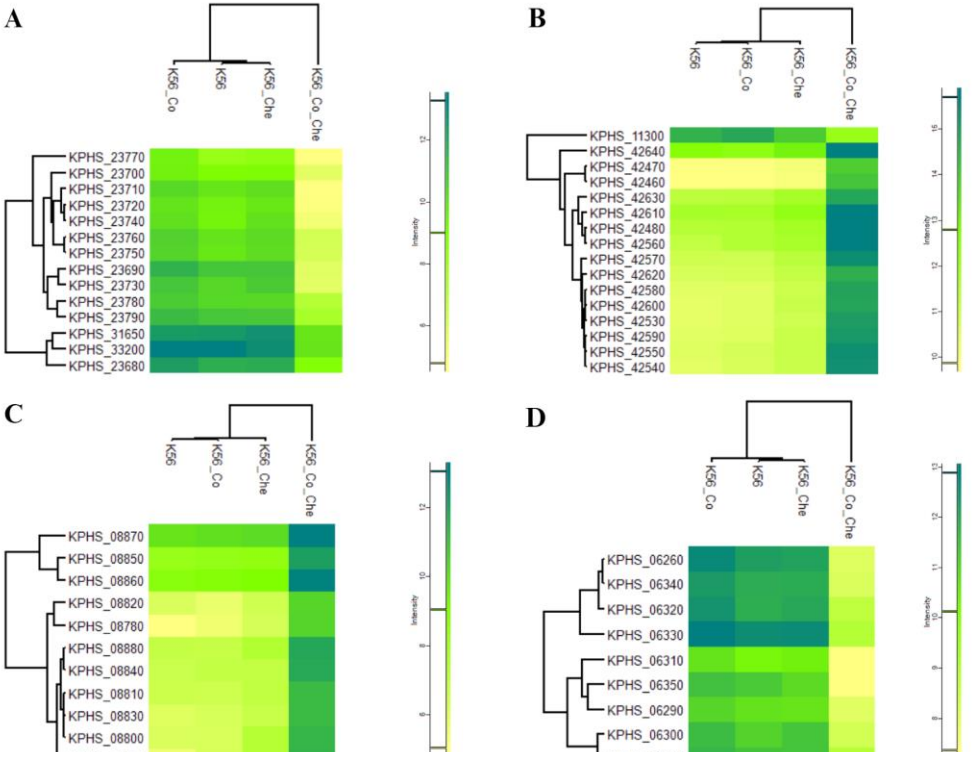

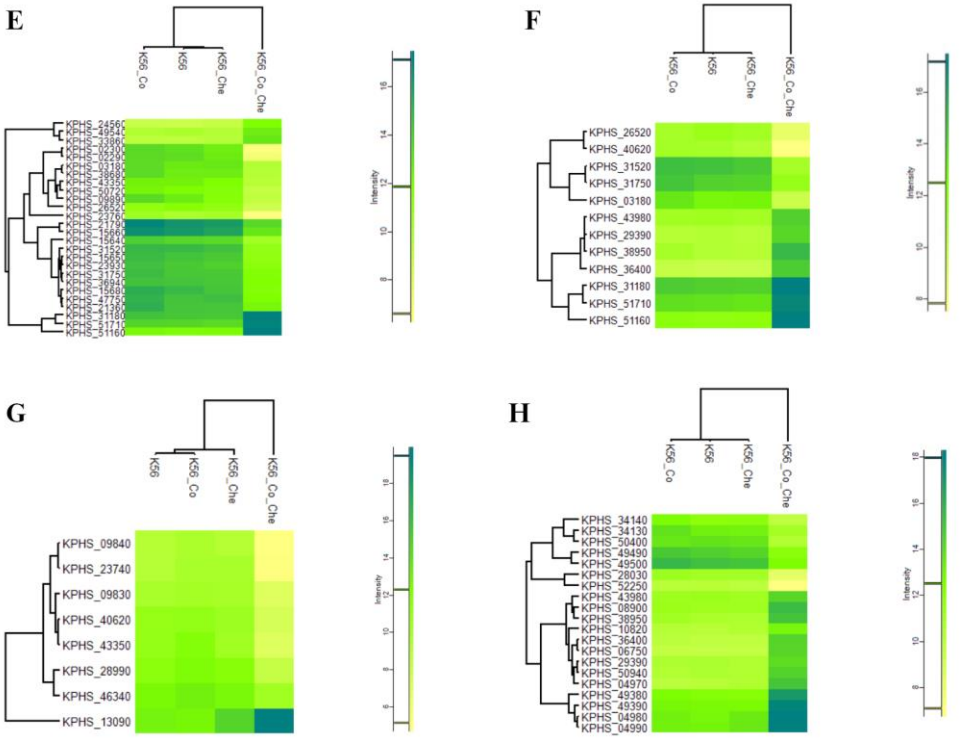

Figure 14. Heatmaps of diverse pathways. (A) KPHS_23690 and KPHS_23710 were remarkable decreased in phenylalanine metabolism. (B) The colistin and chemical #3 therapy significantly enhanced the expression of porphyrin metabolism genes, KPHS_42470 and KPHS_42460 except KPHS_11300. Their annotation are adenosylcobinamide kinase/adenosylcobinamide-phosphate guanylyltransferase and nicotinate-nucleotide-dimethylbenzimidazole phosphoribosyltransferase and protoheme IX farnesyltransferase. (C) The combo treatment resulted in enhanced the gross expression of type II secretion system (T2SS). Under the colistin condition, the pullulanase I protein (KPHS_08820) marginally decreased expression compared to the control one. (D) Colistin and chemical #3 treatment brought a reduction in overall tyrosine metabolism. With colistin treatment, 4-hydroxyphenlacetate catabolism (KPHS_06330) and 4-hydroxyphenlacetate catabolism (KPHS_06260) were significantly improved and involved in phenylacetate degradation. (E) The combination treatment causes significant decline isocitrate lyase (KPHS_02300), malate synthase (KPHS_02290), and 3-hydroxy butyryl-CoA dehydrogenase (KPHS_23760) for carbon metabolism. Oppositely, pyruvate kinase (KPHS_31180), triosephosphate isomerase (KPHS_51710), and phosphoglyceromutase (KPHS_51160) were raised. (F) Under the combination condition, acetyl-CoA synthetase (KPHS_03180), glyceraldehyde-3-phosphate dehydrogenase (KPHS_26520), and lactaldehyde dehydrogenase (KPHS_40620) were reduced in the glycolysis or gluconeogenesis pathway.

(G) Compared to the single or control groups, the combination treatment dramatically increased the expression of lysine decarboxylase 1 (KPHS_13090). Conversely, glutarate 2-hydroxylase (KPHS_09840) and enoyl-CoA hydratase-isomerase (KPHS_23740) were decreased in lysine degradation. (H) After combination treatment, trehalose (maltose)-specific PTS system component IIBC (KPHS_04990) was up, while potential phosphotransferase system EIIC (KPHS_52250) was down in starch and sucrose metabolism.

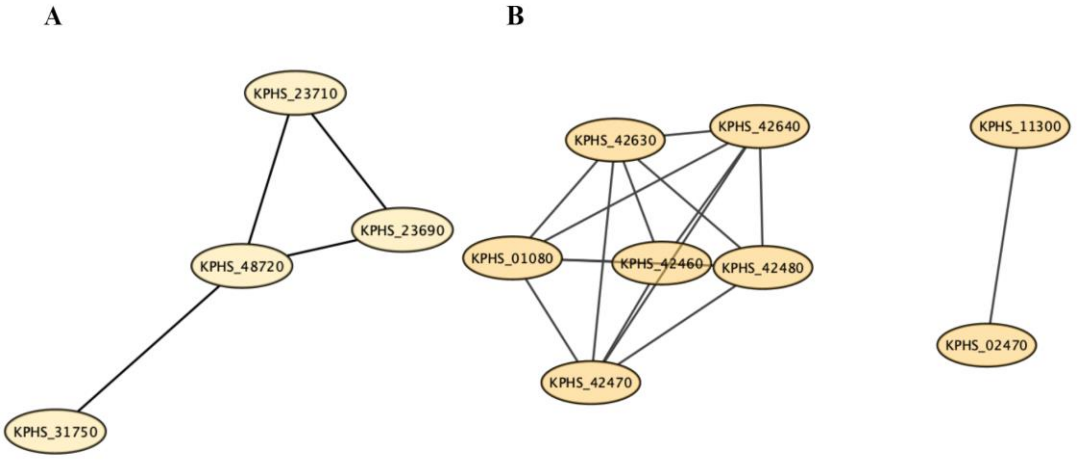

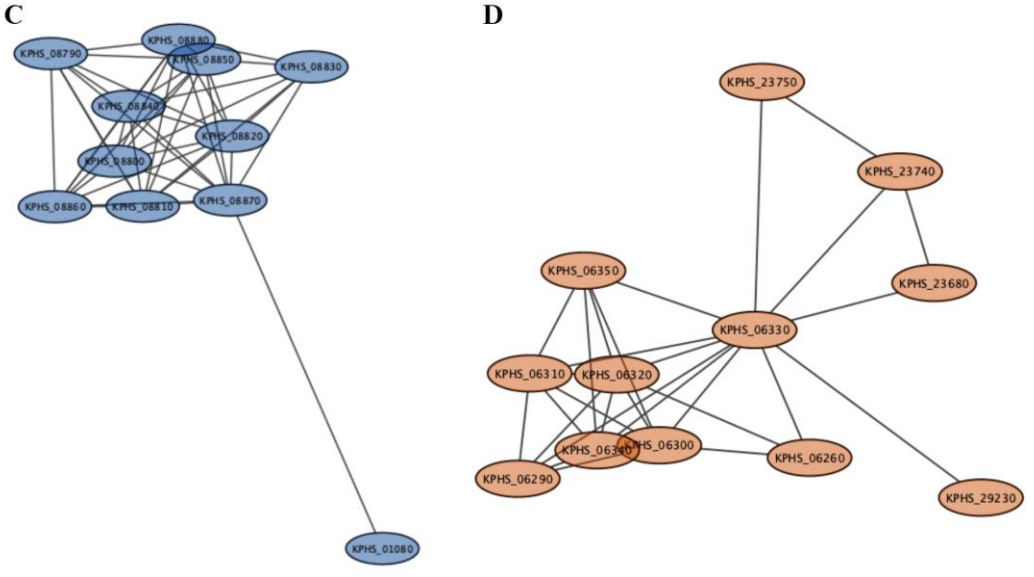

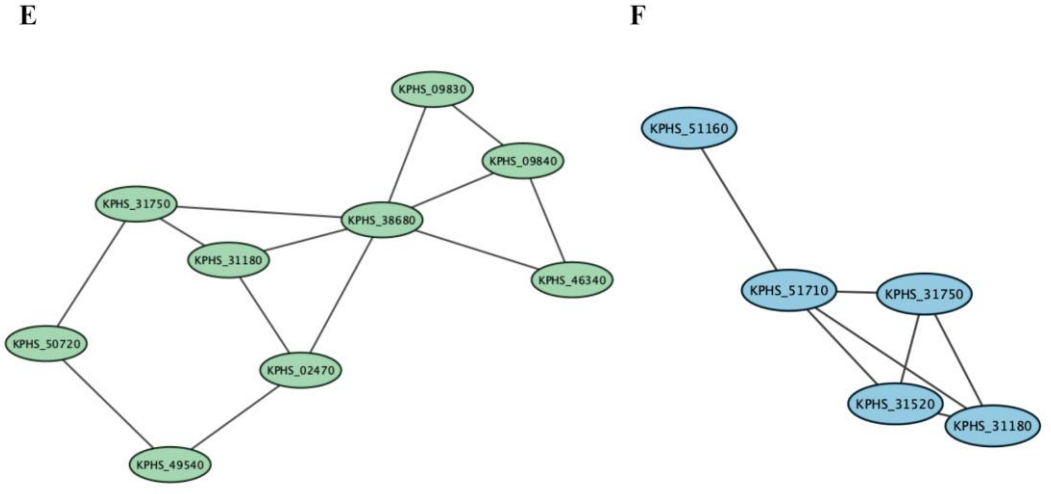

G

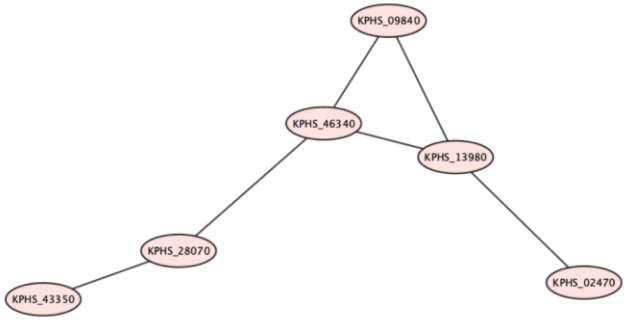

H

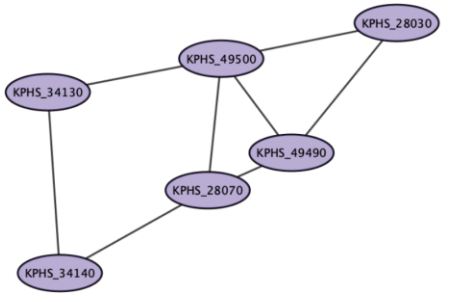

Figure 15. Functional networks form with noncoding RNA-associated genes and DEGs. (A) From porphyrin metabolism, downregulated KPHS_48720 is linked to KPHS_23690 and KPHS_23710. KPHS_48720 is also connected to KPHS_31750, related to the RNA thermometer, glucose or glyconeogenesis, and carbon metabolism. (B) Positively response KPHS_42470, KPHS_42460, cobyric acid synthase (KPHS_42480), cobyric acid a, c-diamide synthase (KPHS_42640), and cobalamin biosynthesis protein (KPHS_42630) are functionally associated with an outer membrane transporter (KPHS_01080) for vitamin B12 (cobalamin) in porphyrin metabolism. (C) The cobalamin riboswitch-associated KPHS_01080 is linked to the DEGs. (D) A network includes the bifunctional aldehyde dehydrogenase/enoyl-CoA hydratase (KPHS_23680), the 4-hydroxyphenlacetate degradation bifunctional isomerase/decarboxylase C-terminal subunit (KPHS_06340), 4-hydroxyphenlacetate catabolism (KPHS_06310), 4-hydroxyphenlacetate catabolism (KPHS_06350), and KPHS_06330. (E) The upregulated gluconate kinase (KPHS_49540) and pyruvate kinase (KPHS_31180) and the downregulated putative kinase (KPHS_50720) and transaldolase kinase (KPHS_38680) are functionally associated with the downregulated 6-phosphofructokinase (KPHS_31750) based on the Database for Annotation, Visualization, and Integrated Discovery (DAVID). In the functional network, glucose-6-phosphate (KPHS_02470), hypothetical protein (KPHS_09830), hypothetical protein (KPHS_09840), and putrescine (KPHS_46340) were present. KPHS_02470 is associated with the lysine riboswitch and connected to KPHS_38680 in the pentose phosphate pathway.

(F) The integrative network is generated by low levels of phosphoenolpyruvate synthase (KPHS_31520) and 6-phosphofructokinase (KPHS_31750), with high triosephosphate isomerase (KPHS_51710), pyruvate kinase (KPHS_31180), and phosphoglyceromutase (KPHS_51160). (G) In the metabolism of phenylalanine, KPHS_23740 is associated with the enoyl-CoA hydratase (KPHS_23680). According to ANNOgesic analysis, KPHS_28070 is the target gene of a novel noncoding sRNA. It is interconnected to the putrescine aminotransferases (KPHS_46340) and acetyl-CoA acetyltransferase (KPHS_43350) with downregulation. Through the carboxylate-amine ligase (KPHS_13980), positively expressed glucose-6-phosphate isomerase (KPHS_02470), and negatively expressed KPHS_09840, and KPHS_46340 form an indirect network. (H) Minor downregulation of alpha-trehalose-phosphate synthase (KPHS_34130) and trehalose-6-phosphate phosphatase (KPHS_34140). The first gene is associated with decreased KPHS_31750 and increased KPHS_31180 expression levels. KPHS_34140 is also connected to the general stress protein (KPHS_28070).

Table 5. Genomic RNA thermometer activity

#ID	Genome	Strand	Associated_CDS	Start_genome	End_genome	Rfam_ID	Rfam_name	E_value	Score	Start_align	End_align
RNA_thermometer_1602	NC_016845.1	+	KPHS_31750	3159385	3159509	RF01859	Phe_leader	4.10E-16	74.1	1	125
RNA_thermometer_1660	NC_016845.1	+	KPHS_33570	3335790	3336228	RF01766	cspA	1.70E-41	145.6	1	439
RNA_thermometer_37	NC_016845.1	+	KPHS_00820	81970	82028	RF01859	Phe_leader	3.10E-05	23.6	1	37
RNA_thermometer_39	NC_016845.1	+	KPHS_00860	90457	90536	RF01859	Phe_leader	5.60E-06	27.6	1	80
RNA_thermometer_606	NC_016845.1	+	KPHS_11580	1215650	1215709	RF01859	Phe_leader	4.80E-06	27.3	1	60
RNA_thermometer_1537	NC_016845.1	+	KPHS_30060	2996291	2996377	RF01859	Phe_leader	0.00021	20.7	1	36
RNA_thermometer_1593	NC_016845.1	+	KPHS_31510	3134900	3134984	RF01859	Phe_leader	4.90E-05	23.4	1	85
RNA_thermometer_19	NC_016846.1	-	KPHS_p200210	7230	7296	RF01804	Lambda_thermo	0.00067	14.5	1	67

In the combination condition, three distinct RNA thermometers were found, along with eight related genes. For a phenylalanine leader peptide RNA thermometer, KPHS_31750 has the coding sequence predicted by ANNOgesic.

3.2.4. Regulation of cobalamin in porphyrin metabolism

To explore pathways from individual pathways to group pathways, the involvement of regulatory noncoding RNAs is crucial for analyzing pathway relationships (Figures 16 and 17). Noncoding RNAs work at specific parts to connect the circuit without disturbance. The location of the cobalamin riboswitch is between 117353 and 117540, as predicted by the ANNOgesic tool (Table 6). It is upstream of KPHS_01080, which acts as a cobalamin transporter as well as bacteriocins and bacteriophages receptors[49-51]. There are strong upregulations of other cobalamin biosynthesis genes, whereas TonB-dependent KPHS_01080 is not (Figure 18A and 18B from BiCU). Hence, gene expression is regulated by the cis-regulatory riboswitch via a negative feedback loop (https://rfam.org).

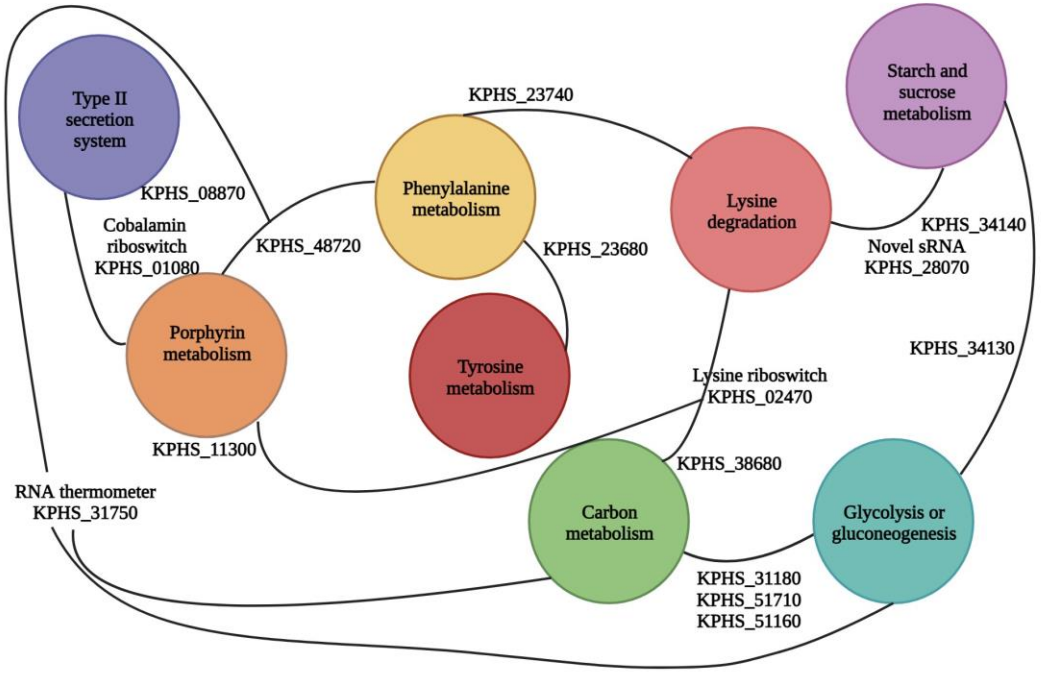

Figure 16. Network analysis of pathways. Nodes and lines indicate specific paths and relationships. KPHS_48720 from porphyrin metabolism links associated genes, KPHS_23690, KPHS_23710, and the decreasing KPHS_31750. Porphyrin metabolism-related KPHS_01080 is functionally connected with the pullulanase D protein (KPHS_08870) from the T2SS. A lysine riboswitch-related KPHS_02470 has an exceeding expression, which leads to KPHS_11300 decline. Additionally, KPHS_28070 is associated with KPHS_34140. During carbon metabolism, glycolysis, and gluconeogenesis, KPHS_31180, KPHS_51710, and KPHS_51160 increase.

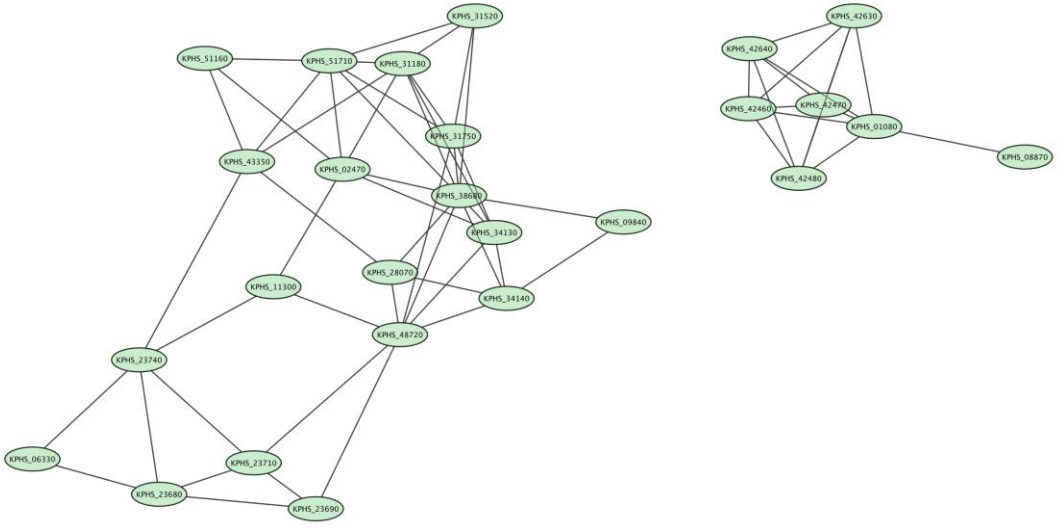

Figure 17. Integrated functional network.

Table 6. Genomic riboswitch activity

#ID	Genome	Strand	Associated_CDS	Start_genome	End_genome	Rfam_ID	Rfam_name	E_value	Score	Start_align	End_align
riboswitch_52	NC_016845.1	+	KPHS_01080	117353	117540	RF00174	Cobalamin	1.40E-27	94.5	1	188
riboswitch_137	NC_016845.1	+	KPHS_02470	286829	287064	RF00168	Lysine	2.50E-38	132.1	1	236
riboswitch_1439	NC_016845.1	+	KPHS_27520	2757256	2757357	RF00059	TPP	5.10E-16	69.5	1	102
riboswitch_1659	NC_016845.1	+	KPHS_33510	3332260	3332362	RF00080	yybP-ykoY	4.50E-13	44.3	1	103
riboswitch_1774	NC_016845.1	+	KPHS_36130	3630799	3630896	RF00059	TPP	7.80E-16	68.6	1	98
riboswitch_2046	NC_016845.1	+	KPHS_42660	4297879	4298057	RF00174	Cobalamin	2.90E-29	100.1	1	179
riboswitch_2184	NC_016845.1	+	KPHS_45820	4607336	4607487	RF00050	FMN	2.50E-33	125.2	1	152
riboswitch_10	NC_016845.1	+	KPHS_00290	35097	35170	RF00519	suhB	5.60E-05	21	1	74
riboswitch_39	NC_016845.1	+	KPHS_00860	90473	90552	RF00516	ylbH	3.70E-05	21.1	1	80
riboswitch_1426	NC_016845.1	+	KPHS_27170	2724825	2724923	RF00442	ykkC-yxkD	0.00049	16.4	1	99
riboswitch_1610	NC_016845.1	+	KPHS_31920	3173316	3173390	RF00519	suhB	0.00017	19.1	1	75
riboswitch_105	NC_016846.1	+	KPHS_p201070	74176	74242	RF01051	c-di-GMP-I	0.00022	19.8	1	67

Under combination therapy, 10 riboswitches and 12 related genes were predicted using ANNOgesic analysis. KPHS_01080 and KPHS_02470 were related to the cobalamin and lysine riboswitches, respectively.

A

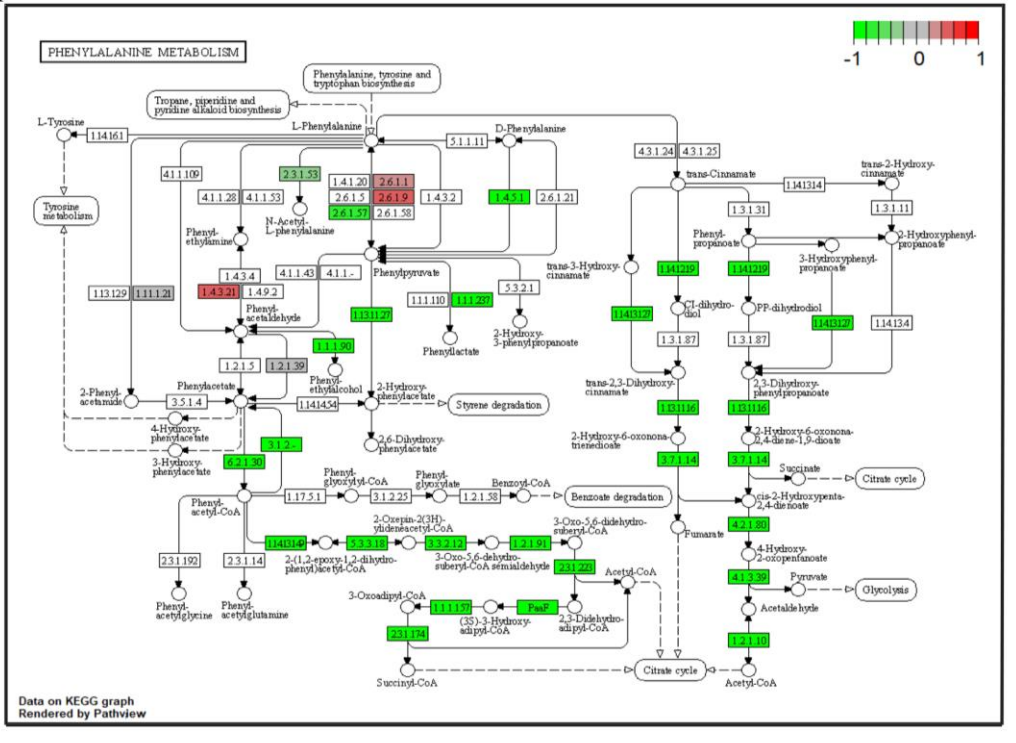

B

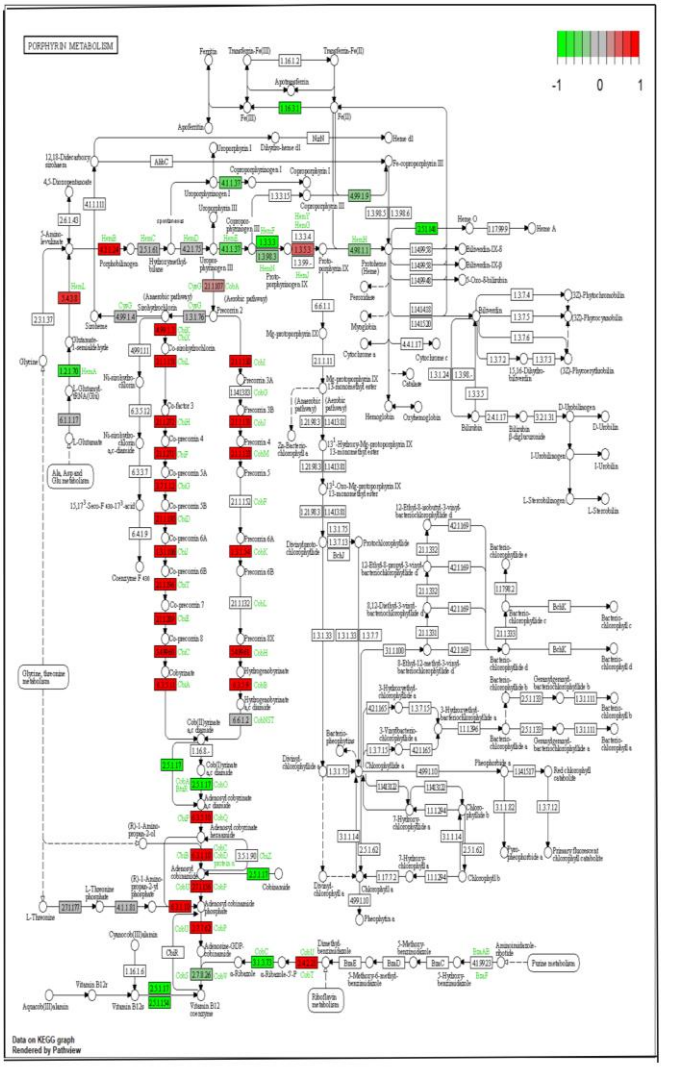

Figure 18. The Kyoto Encyclopedia of Genes and Genomes (KEGG) describes metabolic pathways. (A) Phenylalanine metabolism. The citrate cycle produced fewer intermediates, including acetyl-CoA and succinyl-CoA, as per the KEGG study. (B) Porphyrin metabolism. The anaerobic and aerobic de novo pathway reacts favorably, and vice versa, the salvage (transporter) pathway reacts unfavorably.

3.2.5. Improved nutrient uptake with the Type II Secretion System

Through the action of local and long-range effectors, the T2SS facilitates nutrition absorption from the external environment[52]. The T2SS complex is composed of multiple proteins to facilitate the transport of external factors. They are exported through the periplasm to the cell surface[53] with upregulation of multiple T2SS parts (Figures 14C and 19). Pullulanase D protein (KPHS_08870) uses a sec transporter for a proper function[54]. In a signal-sequence-dependent pathway, proteins move via cell membranes[55-57]. Pullulanase I protein (KPHS_08820) is a component of the pseudopilin complex that participates in protein secretion[58]. The proteins pullulanase E (KPHS_08860) and pullulanase L (KPHS_08790) have the same function as toxins and hydrolytic enzyme production. For secretion of toxins and hydrolytic enzymes (https://uniprot.org), the first protein acts as an ATPase[59], and the second one acts as an inner membrane element to open and close pores[60].

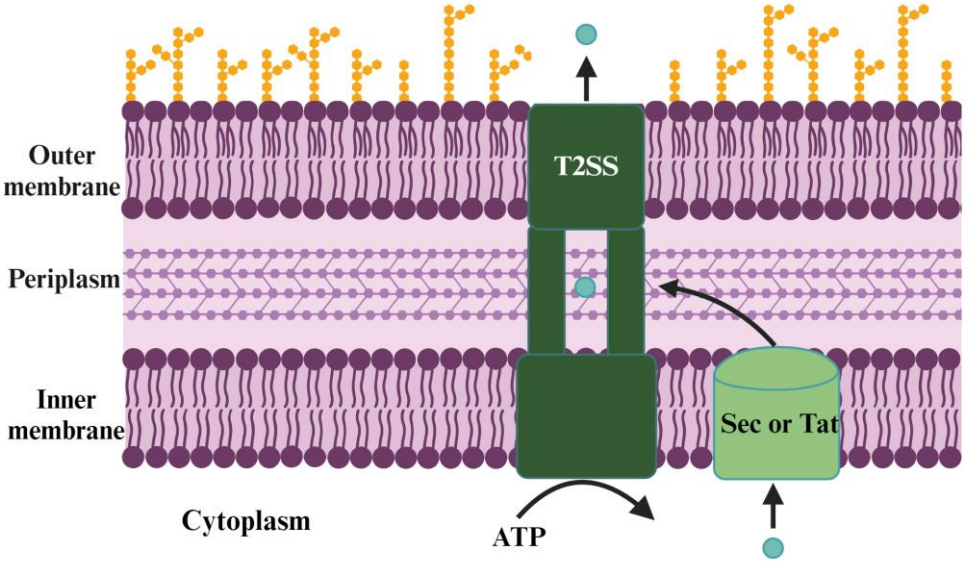

Figure 19. Mechanism of the type II secretion system.

3.2.6. Similarities between the tyrosine and phenylalanine pathways

Tyrosine metabolism also interacts with phenylalanine. Both pathways exhibit a downregulated pattern and an adjacent relationship of aromatic amino acids. After combination therapy exposure, KPHS_06330 is functionally connected to PaaN phenylacetic acid degradation protein (KPHS_23680)[61] for 4-hydroxyphenyl acetic acid degradation[62] (Figure 15D).

3.2.7. Role of regulatory RNA thermometers

In carbohydrate metabolism, the KPHS_31750 and phenylalanine leader peptide attenuator work for specific activities such as the carbon metabolism, glucose, or gluconeogenesis pathways. DAVID identifies functional similarities among pyruvate kinase, gluconate kinase, and 6-phosphofrucokinase (KPHS_31180, KPHS_49540, and KPHS_31750)[63,64]. KPHS_31180 converts pyruvate in glycolysis[65], while KPHS_51160 plays a role in glucose-related catabolism. Upregulated KPHS_49540 is implicated in thermoresistant and thermosensitive isozymes[66] during carbohydrate metabolism. Specifically, KPHS_49540 catalyzes phosphoryl transfer to generate a gluconate-6-phosphate precursor for gluconate metabolism[67,68]. Ultimately, carbon metabolism, glycolysis, and gluconeogenesis are controlled by the RNA thermometer. (Figure 15E). Triosephosphate isomerase (KPHS_51710) transforms dihydroxyacetone phosphate to glyceraldehyde-3phosphate dehydrogenase (GAPDH)[69] for energy to survive. The enzyme phosphoenolpyruvate synthase (KPHS_31520) has a function for phosphorylation. The connection among unchanged glutamate dehydrogenase (KPHS_21050), the RNA thermometer-associated KPHS_31750, and the lysine riboswitch-associated KPHS_02470 represents interactions with regulators (Figure 20). Conserved lysine residues of glutamate and phenylalanine share structural and functional similarities for catalytic activity (https://ebi.ac.uk/interpro). There is an exception: the relationship

between cold shock protein (KPHS_33570) and related genes of upregulation is not supported by the functional network KlebNet. One probable explanation for this contradiction (Table 5) is that our ANNOgesic analysis was performed based on RNA-seq, neither differential RNA-seq nor term-seq. Anticipation of bacterial transcription start sites, processing sites, and promoters is excluded from analysis. Continued research is required to resolve this unsolved difference.

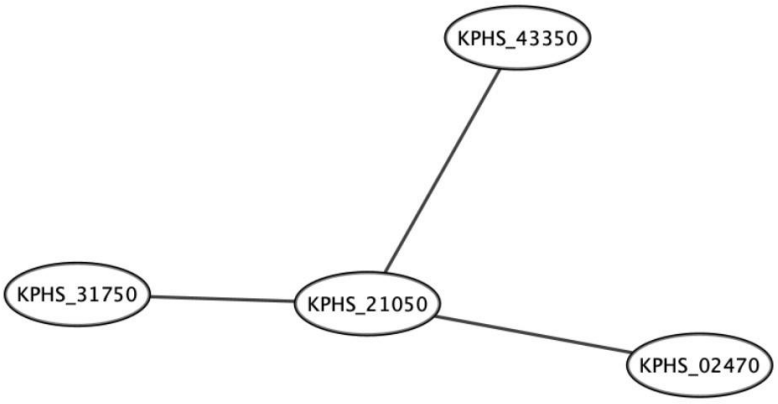

Figure 20. Genes related to the RNA thermometer of the phenylalanine leader peptide.

3.2.8. The carbon metabolism and glycolysis/gluconeogenesis relationship

Carbon metabolism, glycolysis, and gluconeogenesis are closely related. Downregulated genes such as isocitrate lyase (KPHS_02300), malate synthase (KPHS_02290), and 3-hydroxybutyryl-CoA dehydrogenase (KPHS_23760) in the anaerobic glyoxylate bypass pathway facilitate glucose production from fatty acids. Oppositely, three upregulated genes, KPHS_31180, KPHS_51710, and KPHS_51160, show considerable expression during carbon metabolism, glycolysis, or gluconeogenesis (Figures 14E and 14F). Anaerobic energy generation seems to be boosted through glycolysis, or gluconeogenesis, rather than the glyoxylate cycle.

3.2.9. Glycolysis or gluconeogenesis movement to gain energy for survival

Glycolysis synthesizes glucose as a carbon source, and the gluconeogenesis pathway is a reversal of it[70] (https://biocyc.org). The reduced expression of acetyl-CoA synthetase (KPHS_03180) may lead to lower acetyl-CoA levels. Decreased aldehyde dehydrogenase negatively affects ethanol-derived acetate generation after exposure to combination therapy[71]. The reduction of bacterial pathogenicity is related to lower expression of GAPDH (KPHS_26520)[72]. Upregulated glycoside hydrolase KPHS_36400 promotes the metabolism of starch and sucrose (Figure 14F). Three KPHS_29390, KPHS_43980, and KPHS_38950 (6-phospho-beta-glucosidase) genes are involved in breaking down glycosidic linkages in cellulose and carbohydrate processes.

3.2.10. Lysine interruption disturbs the fatty acid membranes

Figure 15G shows a functional network that works in carbon metabolism and lysine degradation. Lysine plays a role in the catalytic mechanism. For amino acid metabolism, KPHS_13090, known as lysine decarboxylase 1, decarboxylates lysine[73]. Downregulated glutarate 2-hydroxylase, or carbon starvation-induced protein (KPHS_09840), leads to the breakdown of L-lysine by catalyzing glutamate hydroxylation and producing L-2-hydroxyglutarate (https://uniprot.org). Acetyl-CoA acetyltransferase (KPHS_43350) downregulation contributes to fatty acid breakdown. In phenylalanine metabolism and lysine degradation, downregulation of enoyl-CoA hydratase-isomerase (KPHS_23740) occurs as well. The breakdown of unsaturated fatty acids is catalyzed by enoyl-CoA delta isomerase[74]. The enzyme affects phospholipid membrane alteration and fatty acid production, contributing to membrane disruption[75]. Despite that, a notable morphological difference was not observed with transmission electron microscopy (TEM) (Figure 21). It may cause a two-fold decrease from the susceptibility determination value (MIC). The ANNOgesic identified a new sRNA with a target gene, KPHS_28070 (stress-induced bacterial acidophils repeat motif) (Figure 22). The downregulated gene is associated with acid stress and inhibition of bacterial growth without destruction[76]. Figure 15G displays that the glucose-6-phosphate isomerase (KPHS_02470) and carboxylate-amine ligase (KPHS_13980) have an indirect functional association. The

KPHS_02470 may work under the lysine riboswitch during the lysine degradation process.

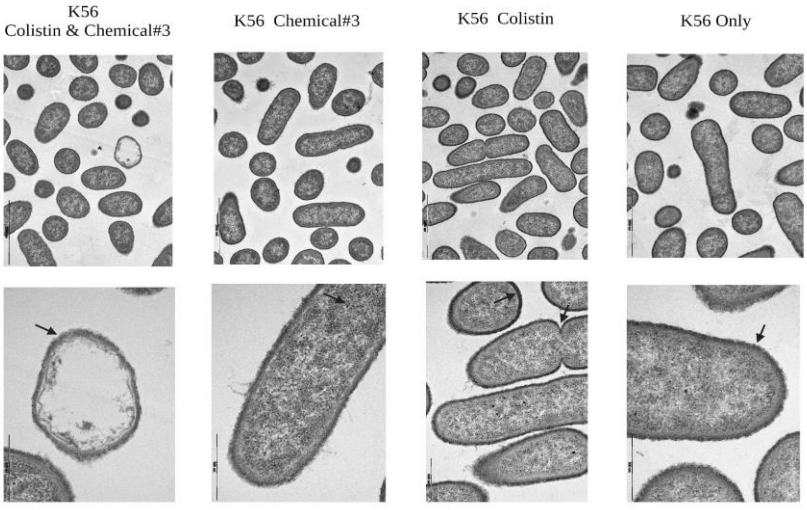

Figure 21. Transmission electron microscopy. At a concentration of 0.25 μg/ml colistin with 0.5 μg/ml chemical #3, no substantial morphological changes were found.

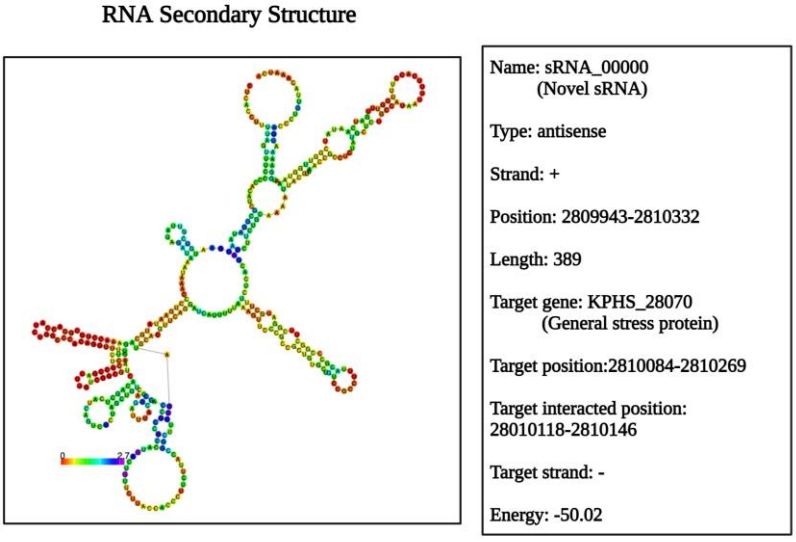

Figure 22. ANNOgesic identified a novel sRNA. The cis-acting antisense RNA has 389 nucleotides to modulate gene expression with negatively binding energy. It is transcribed on the opposite strand of KPHS_28070 (the stress-induced acidophilic repeat motif-containing protein).

3.2.11. Bacterial durability of starch and sucrose metabolism

During stressful conditions, downregulated trehalose-6-phosphate phosphatase (KPHS_34140) produces trehalose and orthophosphate by regulating the dephosphorylation of trehalose-6-phosphate[77] (Figure 14H). Conversely, upregulated trehalose (maltose)-specific PTS component IIBC KPHS_04990 affects the carbohydrate transport system through the trehalose-6-phosphate breakdown into glucose and glucose 6-phosphate. Bacteria maximize their growth rate by reducing carbon source utilization and increasing glucose synthesis[78]. Enhanced expression of glycogen phosphorylase (KPHS_49390) indicates glycosidic bond formation. Declined putative glycosidase (KPHS_28030) affects glycosidic bond hydrolysis in carbohydrate metabolism. The net trend demonstrates a rise in the formation of glycosidic bonds. Higher trehalase 6-P hydrolase (KPHS_04980) expression defends against hyperosmotic and thermal stress[79]. A component of the phosphoenolpyruvate-dependent sugar PTS, putative PTS, EIIC (KPHS_52250) promotes metabolism and transcription[80] by taking charge of sugar transport and phosphorylation[81]. The downregulation of the gene results in less sugar intake. It is similar to the upregulated KPHS_04990. Both downregulated KPHS_52250 and the cellulose synthase catalytic subunit KPHS_50400 stop nutrition uptake and starch saccharification[82]. KPHS_52250 and KPHS_29390, KPHS_43980, and KPHS_38950 have interactions (Figure 14F). These

upregulated glycoside hydrolase genes work in the glucose or gluconeogenesis pathway (Figure 14H).

3.3. Experimental approaches

In Venn diagram Figure 23, only 2 genes (KPHS_36020 xylulokinase and KPHS_36030 D-arabinol dehydrogenase) are expressed in all three conditions (K56 vs. K56_Colistin, K56 vs. K56_Chemical #3, K56 vs. K56_Colistin_Chemical #3). The two Genes are downregulated under all conditions except when they're upregulated in colistin-only. The real-time qPCR with the TaqMan probe was performed to validate the transcriptome. Yellow and green bars represent the KPHS_36020 gene and the endogenous gene rpoD (RNA polymerase sigma factor), respectively (Figure 24) (Table 7). Expression declined in the order of K56_Colistin, K56 only, K56_Chemical#3, and K56_Colistin_Chemical#3. ATP measurement was determined to observe bacterial reactions and viability under stressful environments. The same order was observed for the ATP measurement (Figure 24). The overall ATP trend stays at a similar level with minimal changes. There is oxidoreductase activity associated with KPHS_36030 gene is expressed in all three conditions. However, the gene expression was undetermined, possibly because of inappropriate primers for forward, reverse, and TaqMan probes.

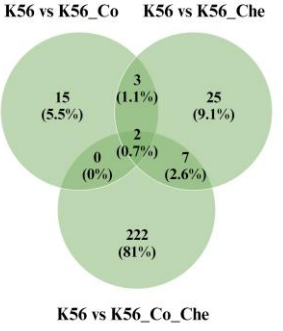

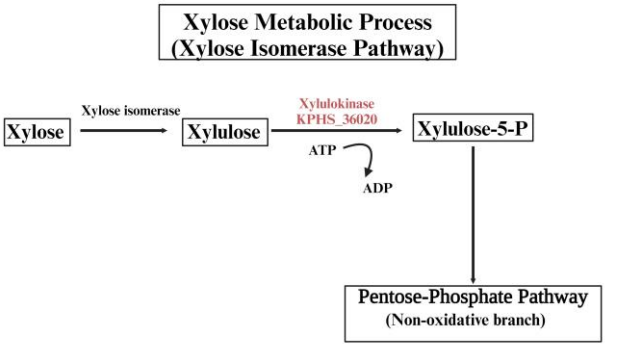

Figure 23. The two common genes in the three different conditions and the K56_Colistin mechanism.

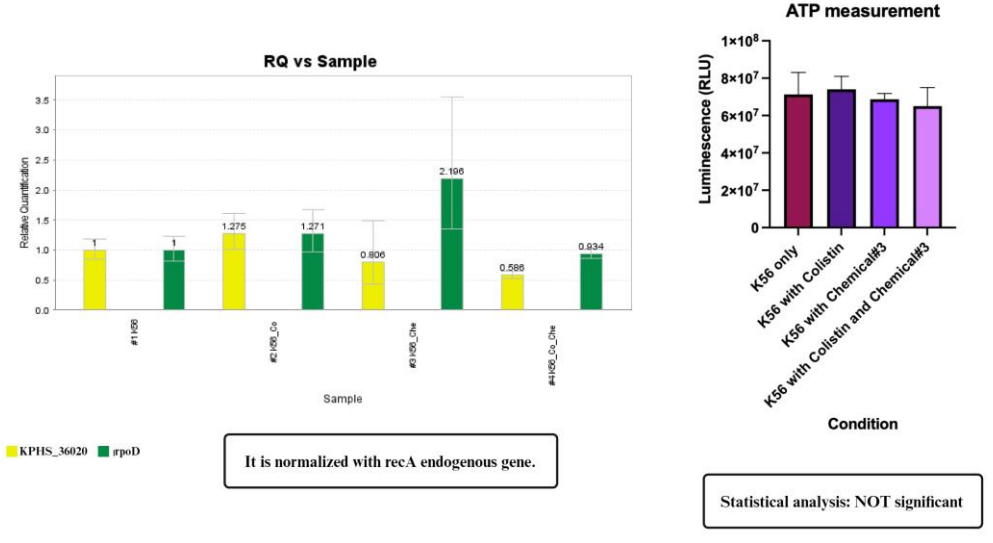

Figure 24. Transcriptome validation and bacterial viability determination.

Table 7. Primers and TaqMan probe design

Name	Amplicon Size	Sequence (5' to 3')	Start Position	Strand	Length	Primer Tm	Purity	Modification	Scale
KPHS_36020	121								
	query_L1	AGCTGTTTGCAGTGGTTCTG	895	forward	20	56.05	PAGE		0.05 umol
	query_R1	CGGAGAGATAGGGCAGGAAG	996	reverse	20	56.09	PAGE		0.05 umol
	query_P1	AGCAGCGCCACCTCCGTGGT	928	reverse	20	66.13	HPLC	5'Fam - 3'Tamra	0.05 umol
Housekeeping gene rpoD	129								
	query_L1	TCCGAACGCCGAAGAAGATA	501	forward	20	55.98	PAGE		0.05 umol
	query_R1	TTGTCGTCATCGCTGTTGTC	610	reverse	20	56.01	PAGE		0.05 umol
	query_P1	CGCCACCCACGTTGGCTCCG	531	forward	20	65.79	HPLC	5'Fam - 3'Tamra	0.05 umol

3.4. 2DE gel electrophoresis-based proteome analysis at the protein level

In this section, we only focused on highly expressed proteins in the K56_Colistin_Chemical #3 treatment compared to the K56 control. The six most expressed proteins were decided (Figure 25). Trigger factor (TF), uronate isomerase, elongation factor, thermal unstable (EF-Tu), and beta-lactamase SHV-11 were listed in reducing order (Table 8). Multiple groups (228, 239, and 960) under the same protein EF-Tu with the same accession number (AEW58892.1). Among six the three protein expressions were from the same protein due to the most abundance.

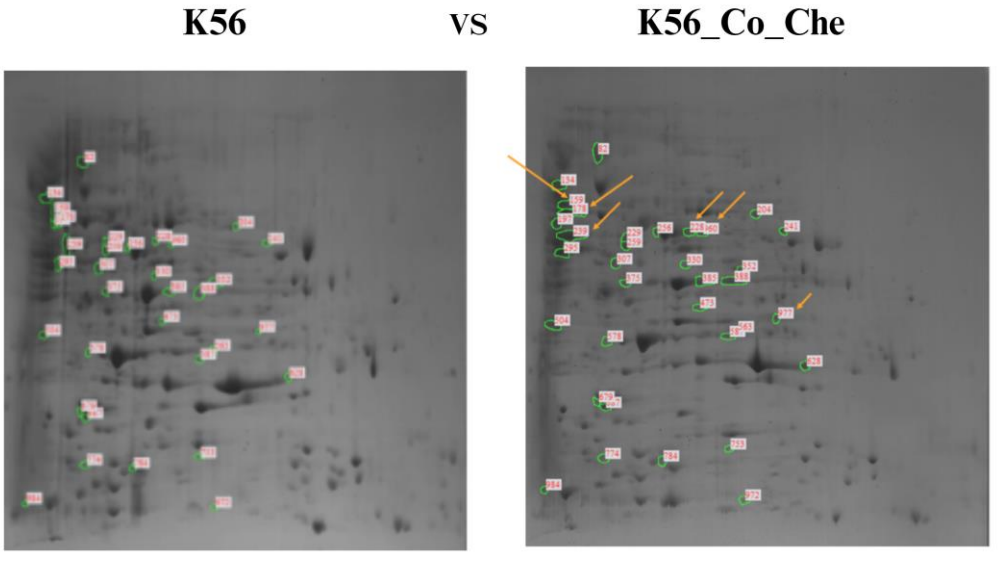

Figure 25. 2DE gel electrophoresis proteomic analysis.

Table 8. LC/MS analysis of 6 major spots

Group number	Protein name (gray p>0.05)	Accession number	Calculated Mr (Da)	Calculated pI	Protein sequence coverage (%)	Protein score
159	Trigger factor [Klebsiella pneumoniae subsp. pneumoniae HS 11286]	AEW59837.1	48097	4.85	51	1523
178	Uronate isomerase [Klebsiella pneumoniae subsp. pneumoniae HS 11286]	AEW63351.1	54148	5.56	58	1735
228	Elongation factor Tu [Klebsiella pneumoniae subsp. pneumoniae HS 11286]	AEW58892.1	43390	5.29	84	1643
239	Elongation factor Tu [Klebsiella pneumoniae subsp. pneumoniae HS 11286]	AEW58892.1	43390	5.29	74	1562
960	Elongation factor Tu [Klebsiella pneumoniae subsp. pneumoniae HS 11286]	AEW58892.1	43390	5.29	61	1297
977	beta-lactamase SHV-11 [Klebsiella pneumoniae subsp. pneumoniae HS 11286]	AEW61220.1	31390	7.77	56	1188

3.5. Cheminformatics at the DNA level

3.5.1. Target identification

3.5.1.1. Pangenome analysis

Roary was used to analyze the prokaryote pangenome of strains K26 and K56, defining presence and absent genes[37]. The pipeline includes research on the evolution of bacterial genomic diversity. K56 lacks peptidoglycan D, D-transpeptidase (ftsL), cold shock-like protein (cspC), PTS system-mannose-specific EII AB, C, and D components (manX, manY, manZ), putative manganese efflux pump (mntP), transcriptional regulator (kdgR), and glycerol-3-phosphate regulon repressor (glpR). K26 contains these genes. The following genes are unique to K56: beta-lactamase SHV-4, SHV_1 (bla_1 and 2), maltoporin (lamB_3), and stable plasmid inheritance protein (flmA) (Table 9). Although similar, these two strains are not identical.

Table 9. Pangenome for presence and absence of K26 and K56

Gene	Non-unique Gene name	Annotation	No. isolates	No. sequences	Avg sequences per isolate	Genome Fragment	Order within Fragment	Accessory Fragment	Accessory Order with Fragment	QC	Min group size nuc	Max group size nuc	Avg group size nuc	KPN26	KPN56
bla_1		Beta-lactamase SHV-4	1	1	1	7	2	15	1	Investigate	242	242	242		KPN56_05313
lamB_2		Maltoporin	1	1	1	66	97	8	1		1379	1379	1379		KPN56_02515
lamB_3		Maltoporin	1	1	1	65	23	2	1		1382	1382	1382		KPN56_02812
group_1873		hypothetical protein	1	1	1	7	1	15	2	Investigate	305	305	305		KPN56_05314
group_1874		hypothetical protein	1	1	1	3	1	23	1	Investigate	305	305	305		KPN56_05315
manX		PTS system mannose-specific EIIAB component	1	1	1	67	190	27	1		971	971	971	KPN26_02244	
bla_2		Beta-lactamase SHV-1	1	1	1	3	2	23	2	Investigate	242	242	242		KPN56_05316
manY		PTS system mannose-specific EIIC component	1	1	1	67	189	27	2		800	800	800	KPN26_02245	

Table 9. Pangenome for presence and absence of K26 and K56

Gene	Non-unique Gene name	Annotation	No. isolates	No. sequences	Avg sequences per isolate	Genome Fragment	Order within Fragment	Accessory Fragment	Accessory Order with Fragment	QC	Min group size nuc	Max group size nuc	Avg group size nuc	KPN26	KPN56
group_21	manZ_1	PTS system mannose-specific EIID component	1	1	1	67	188	27	3		851	851	851	KPN26_02246	
group_22		hypothetical protein	1	1	1	67	187	27	4		458	458	458	KPN26_02247	
mntP		putative manganese efflux pump MntP	1	1	1	67	186	27	5		566	566	566	KPN26_02248	
rlmA		23S rRNA (guanine(745)-N(1))-methyltransferase	1	1	1	67	185	27	6		794	794	794	KPN26_02249	
ftsI_1		Peptidoglycan D,D-transpeptidase FtsI	1	1	1	67	184	27	7		1745	1745	1745	KPN26_02250	
cspC		Cold shock-like protein CspC	1	1	1	67	183	27	8		209	209	209	KPN26_02251	
group_27		hypothetical protein	1	1	1	67	182	27	9		290	290	290	KPN26_02252	
group_28		hypothetical protein	1	1	1	67	181	27	10		239	239	239	KPN26_02253	

Table 9. Pangenome presence and absence of K26 and K56

Gene	Non-unique Gene name	Annotation	No. isolates	No. sequences	Avg sequences per isolate	Genome Fragment	Order within Fragment	Accessory Fragment	Accessory Order with Fragment	QC	Min group size nuc	Max group size nuc	Avg group size nuc	KPN26	KPN56
kdgR_1		Transcriptional regulator KdgR	1	1	1	67	180	27	11		791	791	791	KPN26_02254	
bla		Beta-lactamase SHV-2	1	1	1	25	2	20	1		860	860	860	KPN26_05278	
ribZ_2		Riboflavin transporter RibZ	1	1	1	67	179	27	12		1370	1370	1370	KPN26_02255	
htpX		Protease HtpX	1	1	1	67	178	27	13		884	884	884	KPN26_02256	
group_32		hypothetical protein	1	1	1	42	18	13	1		173	173	173	KPN26_05039	
group_33		hypothetical protein	1	1	1	41	14	11	1		347	347	347	KPN26_05124	
glpR_4		Glycerol-3-phosphate regulon repressor	1	1	1	25	3	20	2		761	761	761	KPN26_05279	
group_35		hypothetical protein	1	1	1	2	1	22	1	Investigate	1487	1487	1487	KPN26_05303	

Table 9. Pangenome presence and absence of K26 and K56

Gene	Non-unique Gene name	Annotation	No. isolates	No. sequences	Avg sequences per isolate	Genome Fragment	Order within Fragment	Accessory Fragment	Accessory Order with Fragment	QC	Min group size nuc	Max group size nuc	Avg group size nuc	KPN26	KPN56
group_36		IS6 family transposase IS26	1	1	1	1	1	24	1	Investigate	704	704	704	KPN26_05311	
group_37		hypothetical protein	1	1	1	72	689				503	503	503		KPN56_00632
group_38		hypothetical protein	1	1	1	70	209	6	1		107	107	107		KPN56_01165
group_39		hypothetical protein	1	1	1	65	1	9	1		221	221	221		KPN56_02774
group_40		hypothetical protein	1	1	1	63	18	4	1		530	530	530		KPN56_03153
flmA		Stable plasmid inheritance protein	1	1	1	50	7	12	1		185	185	185		KPN56_04747
group_42		hypothetical protein	1	1	1	47	2	16	2		1202	1202	1202		KPN56_04940

Table 9. Pangenome presence and absence of K26 and K56

Gene	Non-unique Gene name	Annotation	No. isolates	No. sequences	Avg sequences per isolate	Genome Fragment	Order within Fragment	Accessory Fragment	Accessory Order with Fragment	QC	Min group size nuc	Max group size nuc	Avg group size nuc	KPN26	KPN56
group_43		hypothetical protein	1	1	1	44	1	26	2		1202	1202	1202		KPN56_05120
group_44		hypothetical protein	1	1	1	26	3	7	1		287	287	287		KPN56_05287
group_45		hypothetical protein	1	1	1	4	2	25	1	Investigate	602	602	602		KPN56_05294
group_46		hypothetical protein	1	1	1	4	1	25	2	Investigate	416	416	416		KPN56_05295
group_47		hypothetical protein	1	1	1	8	1	18	2	Investigate	389	389	389		KPN56_05303
group_48		hypothetical protein	1	1	1	8	2	18	1	Investigate	224	224	224		KPN56_05304
group_49		hypothetical protein	1	1	1	6	1	21	1	Investigate	188	188	188		KPN56_05321
group_5257		tRNA-Ala(ggc)	1	1	1	62	6	1	1		75	75	75		KPN56_03760

Table 9. Pangenome presence and absence of K26 and K56

Gene	Non-unique Gene name	Annotation	No. isolates	No. sequences	Avg sequences per isolate	Genome Fragment	Order within Fragment	Accessory Fragment	Accessory Order with Fragment	QC	Min group size nuc	Max group size nuc	Avg group size nuc	KPN26	KPN56
group_5259		tRNA-Ala(ggc)	1	1	1	62	5	3	1		75	75	75	KPN26_02964	
group_5269		tRNA-Lys(ttt)	1	1	1	71	348	14	1		75	75	75		KPN56_00738
group_5271		tRNA-Lys(ttt)	1	1	1	71	347	5	1		75	75	75	KPN26_03824	
group_5298		hypothetical protein	1	1	1	47	3	16	1		494	494	494		KPN56_04941
group_5299		hypothetical protein	1	1	1	44	2	26	1		494	494	494		KPN56_05121
group_5300		hypothetical protein	1	1	1	47	1	10	1		344	344	344	KPN26_04857	
group_5301		hypothetical protein	1	1	1	5	1	17	1	Investigate	344	344	344	KPN26_05323	
group_5305	lamB_2	Maltoporin	1	1	1	66	95				545	545	545	KPN26_04210	
group_5306	lamB_4	Maltoporin	1	1	1	9	1	19	1	Investigate	545	545	545	KPN26_05319	

3.5.1.2. Protein-protein network including specific genes

LamB_3 was chosen as a critical point in this investigation because to its synergy with chemical #3 and colistin during combined treatment. LamB (KPHS_02600) exhibited considerable upregulation in the conditional transcriptome. The four candidate genes of LamB_3 registered with the NCBI were used to identify the target for further study. KPHS_41450 (lamB maltoporin precursor) had the most resemblance to the lamb_3 nucleotide sequence, with a significance value approaching zero (Table 10). Figure 26 shows that KPHS_02600 (maltoporin) forms a physical subnetwork with KPHS_41450 (maltoporin precursor) and KPHS_01080 (btuB vitamin B12 cobalamin outer membrane transporter) in the STRING protein-protein interaction database[83].

Table 10. A nucleotide sequence alignment for target gene identification

Gene	Score (Bits)	E value
KPHS_02600	30.1	0.25
KPHS_11760	29.2	0.37
KPHS_28630	Not found	Not found
KPHS_41450	33.7	0.021

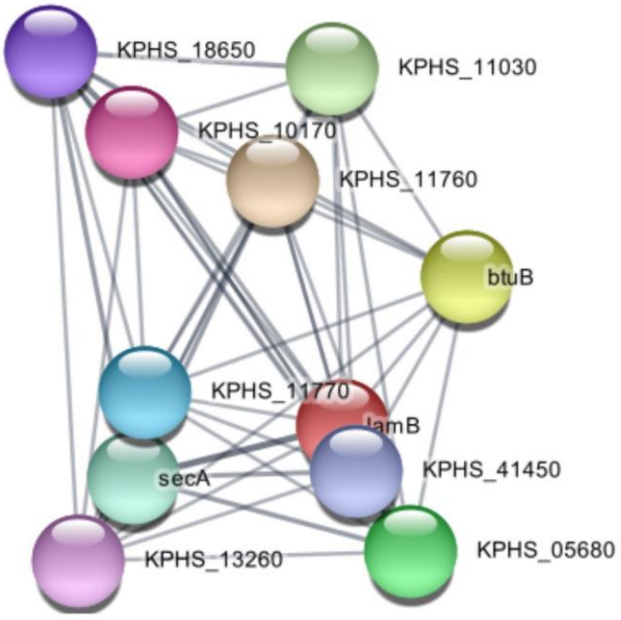

Figure 26. STRING describes protein-protein interactions. The gene KPHS_02600 (lamB) established a physical subnetwork with KPHS_41450 and KPHS_01080 (btuB).

3.5.2. Molecular docking

3.5.2.1. Protein homology modeling

A homology model for molecular docking of proteins (receptors) was built using HOMELETTE. The final model is automodel_def_2MPR_A_1, which has the highest Borda ranking. Next, the active site was discovered to have an 87% pocket probability. The physiochemical properties of the 2MPR protein homology model were analyzed. At pH 4.75, the protein has no net charge, as indicated by its putative pI value of 4.75. The protein is stable, with an instability score of 31.62 (less than 40). The GRAVY value of -0.566 indicates a non-polar protein, as it is negative.

3.5.2.2. Ligands

Seven multiple-ligand complexes were identified for each of the six compounds with meropenem, and chemical #3 with colistin. Meropenem was used to process six chemical candidates from the experimental chemical library screening before moving on to virtual screening. After finely tuned susceptibility tests, only chemical #3 demonstrated an additive impact. Chemical #3, a possible hit molecule, synergized with colistin to inhibit K56.

3.5.2.3. Protein-ligand complexes

The protein (automodel_def_2MPR_A_1) and multiple ligands created a molecular docking complex. The virtual screening of binding affinity results did not accurately reflect the experimental results. Figure 27 illustrates 3D and 2D interactions for viewing and verification.

Chemical #1 with Meropenem

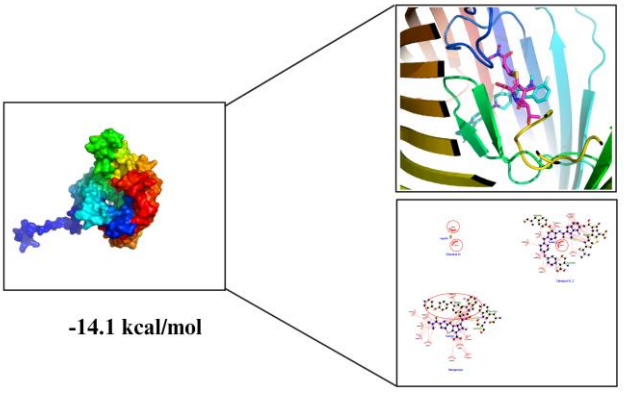

-14.1 kcal/mol

Chemical #2 with Meropenem

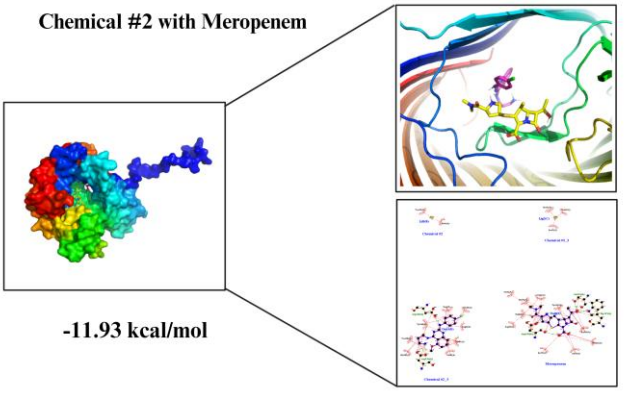

-11.93 kcal/mol

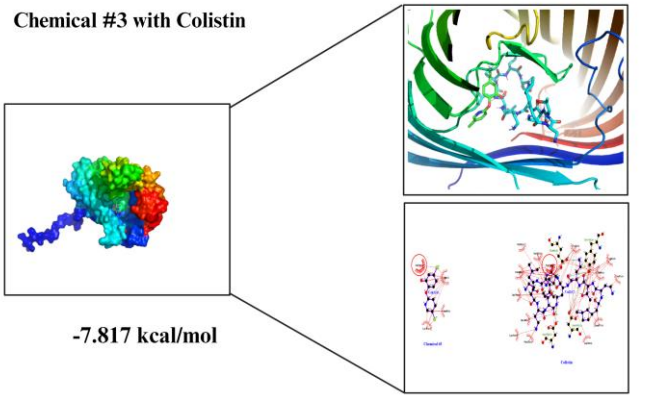

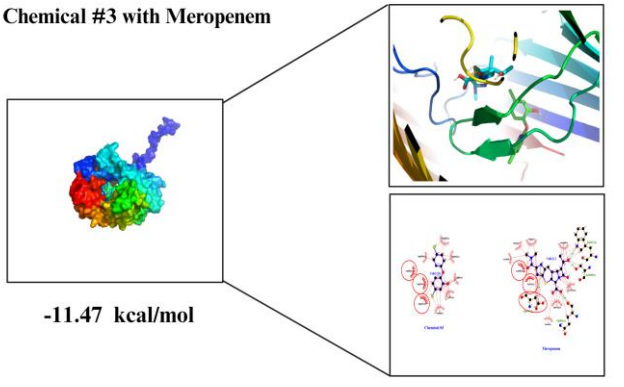

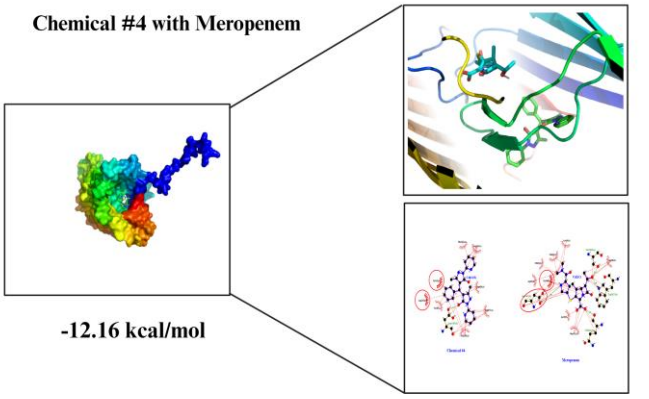

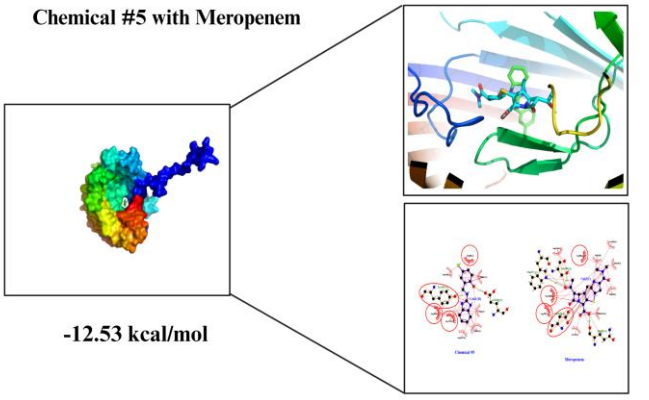

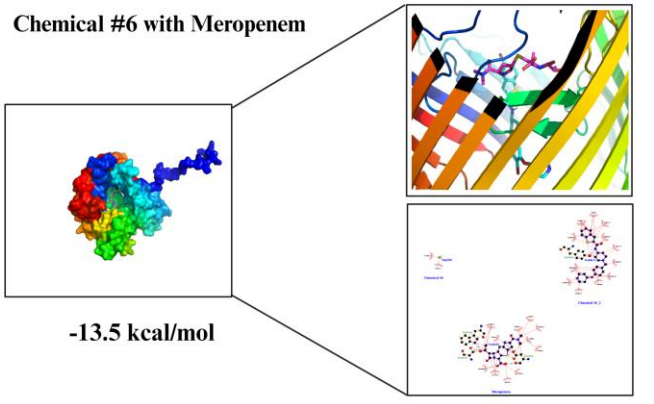

Figure 27. AutoDock Vina analysis displays simultaneous docking of multiple ligands. Chemical #3 demonstrated higher binding affinity values compared to other ligands during molecular docking. Chemical #3 with colistin had the highest binding affinity (-7.817 kcal/mol), followed by chemical #3 with meropenem (-11.47 kcal/mol). Ligand-protein interactions and two-dimensional structures were produced (Contributed by Gyusik Kim).

3.5.3. Structural properties

3.5.3.1. Physiochemical property determination

The physical and chemical features of six chemicals and two antibiotics play a crucial role in predicting drug-likeness and optimizing conditions for modulation[84]. Six physiochemical parameters are represented: octanol/water partition coefficient (LogP, polarity), molecular weight (MW, size), hydrogen bond acceptors (nHAs), donors (nHDs), topological polar surface area (TPSA), and number of rotatable bonds (nRot, flexibility). MW indirectly assesses bioavailability, comparable to ADMET[85]. Table 11 shows computed properties for each chemical. The Drug-Like Soft rule suggests that the ideal MW range is between 100 and 600 Da. However, the polymyxin E antibiotic colistin has higher MW values. In Table 11, chemical #3 has the lowest MW, even lower than meropenem. It is unlikely to require assistance for penetration. Chemical #6 boasts the highest MW. TPSA is the total surface contribution of polar atoms in a molecule[86]. Except for colistin, all seven ligands fall within the optimum range of 0–140. TPSA evaluates transport qualities and is related to bioavailability. The eleventh column shows nRot, which indicates how freely the ligands can rotate. The ideal range is 0–11. Colistin has significantly more rotatable bonds than other chemicals (Table 11). Both chemicals 1 and 6 have high nRot values. The ideal range for the number of nHAs and nHDs is 0 to 12 and 0 to 7, respectively. Except

for colistin, all chemicals fall within these intervals. The high nHA values result in fewer OH and NH bonds compared to O and N bonds. LogP, the final physicochemical parameter, affects both affinity and membrane permeability. Colistin's negative value indicates its hydrophilic nature, high permeability, and effectiveness. Positive numbers imply a ligand is lipophilic, while zero suggests it is biphasic. According to Table 11 (physiochemical characteristics), chemical #3 is less polar and flexible than meropenem. Chemical substances have a shorter MW range compared to antibiotics (Table 11).

Table 11. Physicochemical property determination using ADMETlab

Ligands	MF	LogS	LogD	LogP	MW	Vol	Dense	nHA	nHD	TPSA	nRot	nRing	MaxRing	nHet	fChar	nRig	Flex	nStereo
Chemical 1	C27H33BrClFN4O2	-4.366	3.893	4.354	542.17	498.593	1.087	6	2	58.53	7	5	9	8	0	29	0.241	0
Chemical 2	C18H22Cl3N5O	-2.868	2.947	3.023	357.14	352.108	1.014	6	4	91.55	5	3	10	7	0	19	0.263	0
Chemical 3	C11H7Cl2NO2	-4.069	3.412	3.794	254.99	224.88	1.134	3	1	42.35	2	2	6	5	0	12	0.167	0
Chemical 4	C25H22N6O2	-3.793	1.703	2.891	438.18	447.461	0.979	8	2	101.36	5	5	6	8	0	30	0.167	0
Chemical 5	C14H12ClN3O	-3.174	3.479	3.355	273.07	263.567	1.036	4	3	64.17	2	3	9	5	0	17	0.118	0
Chemical 6	C26H30Br2ClN3O2S	-5.745	3.818	5.204	605.03	502.025	1.205	5	2	53.6	7	5	9	8	0	29	0.241	0
Meropenem	C17H25N3O5S	-1.042	-0.484	-0.663	383.15	361.823	1.059	8	3	110.18	6	3	7	9	0	16	0.375	6
Colistin	C52H98N16O13	-2.35	-2.665	-1.053	1154.75	1160.611	0.995	29	23	490.66	32	1	23	29	0	34	0.941	13

The molecular properties of eight ligands were examined.

3.5.3.2. Similarity comparison

The ChemMine Tool uses a fingerprint similarity approach to calculate chemical structural similarity on a scale of 0 to 1[87]. Fingerprint diversity is compared pair-wise using the Tanimoto index. Fingerprints measure structural diversity using a similarity distribution. Chemicals 1 and 6 had AP Tanimoto and MCS Tanimoto values of 0.658537 and 0.8205 respectively. Chemicals 1 and 6 are close together in the chemical space, suggesting their similarity. Additionally, chemical #5 is close to chemical #3. Figure 28 shows the distribution of chemicals in both 2D and 3D chemical space. The distribution of chemical compounds reveals their diverse physicochemical properties. It demonstrates that the studied ligands had moderate chemical diversity overall.

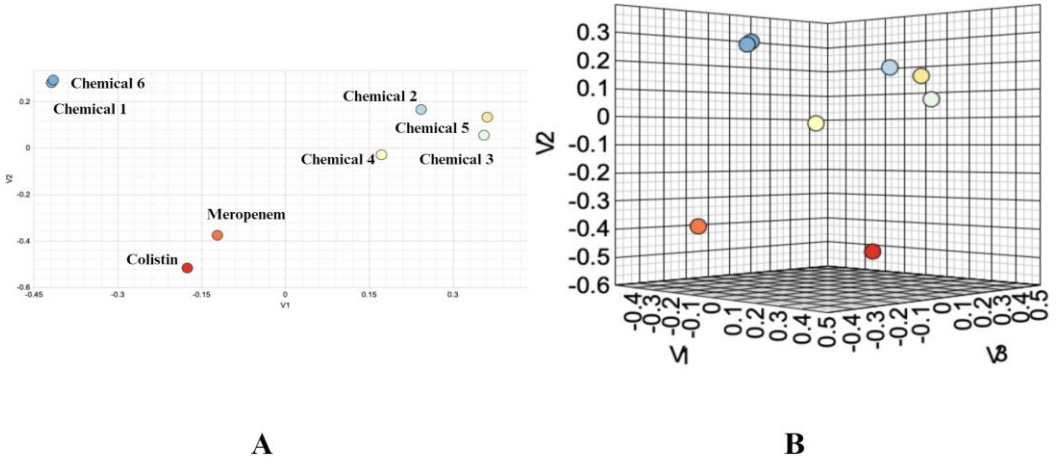

Figure 28. The ligands in the chemical space generated by the ChemMine Tool. Chemical diversity is visualized by reflecting structural and physiochemical features in two and three dimensions.

3.5.4. Molecular dynamics simulation

3.5.4.1. Root-mean-square deviation (RMSD)

RMSD assesses the structural and conformational stability of a simulated system[88]. High RMSD values denote an increase in instability. In detail, it depicts greater deviation in the trajectory as well as remarkable conformational changes in the protein structure. This analysis allows us to study the structural movement in a time-dependent manner. All of the seven combination sets have much more than 3Å RMSD values in the unacceptable range. These imply the great spatial difference[89].

3.5.4.2. Root-mean-square fluctuation (RMSF)

It determines the overall protein stability[90], individual residue flexibility[91], and amino acid mobility[88] through a measurement of positional differences. The RMSF recognizes more dynamical protein regions during a simulation. In general, a high RMSF value is interpreted as indicating more likely loop regions and structural changes with conformational flexibility. As RMSD, RMSF of all 7 different complexes exhibited a similar trend. No major peak or fluctuation was observed in the RMSF residue to identify a specific portion of protein.

3.5.4.3. Hydrogen bonds

This parameter is also important in protein structure because an intramolecular hydrogen bond (non-covalent structural force) estimates the overall complex stability[92]. All seven different complexes had a similar range of hydrogen bonds between 110 and 150.

3.5.4.4. Radius of gyration (Rg)

Radius of gyration characterizes atoms distribution with respect to the center of mass in spatial conformation. In other words, it is the distance from the molecular center of mass during a specific simulation time[93]. This analysis serves to understand the protein's diffusivity[94], compactness[95], and shape. Thus, the high Rg predicts less rigidity, low conformational stability, and low compactness of protein structure[96]. The structural formation process was expressed by this index. Except for chemical #1 with meropenem treatment, other combination treatments have reduced Rg. This is implicated in compacted systems with high stability.

3.5.4.5. Solvent Accessible Surface Area (SASA)

This surface area contacts the solvent through interaction with neighboring solvent molecules[97]. The metric indicates changes in the solvent accessibility[98] and thermodynamic stability[90] of proteins. For instance, high SASA entails high hydrophilicity[99] and is more flexible. Chemical #1 with meropenem complex had a significant

continuous increment in SASA values (Figure 30). It describes low thermodynamic stability[100].

	RMSD	RMSF
Chemical #1 with Meropenem	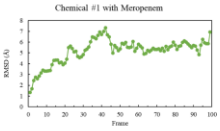	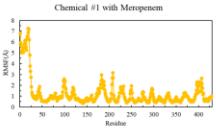
Chemical #2 with Meropenem	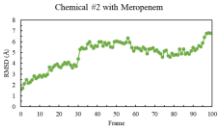	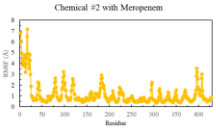
Chemical #3 with Colistin	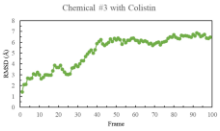	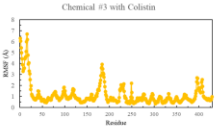
Chemical #3 with Meropenem	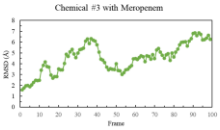	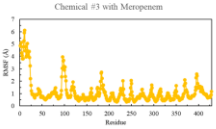
Chemical #4 with Meropenem	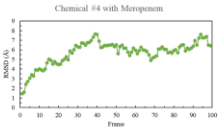	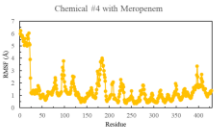
Chemical #5 with Meropenem	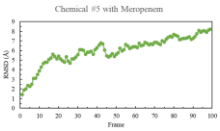	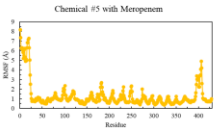
Chemical #6 with Meropenem	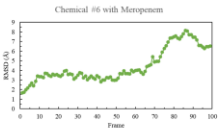	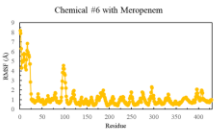

Figure 29. Post MD analysis. These are the parameters, RMSD (RMSD vs. Frame) with backbone atoms and RMSF (RMSF vs. Number of residue) with amino acid residues, of 10 ns trajectories to understand the molecular dynamics simulation. (Contributed by Gyusik Kim and Johnathan Lin)

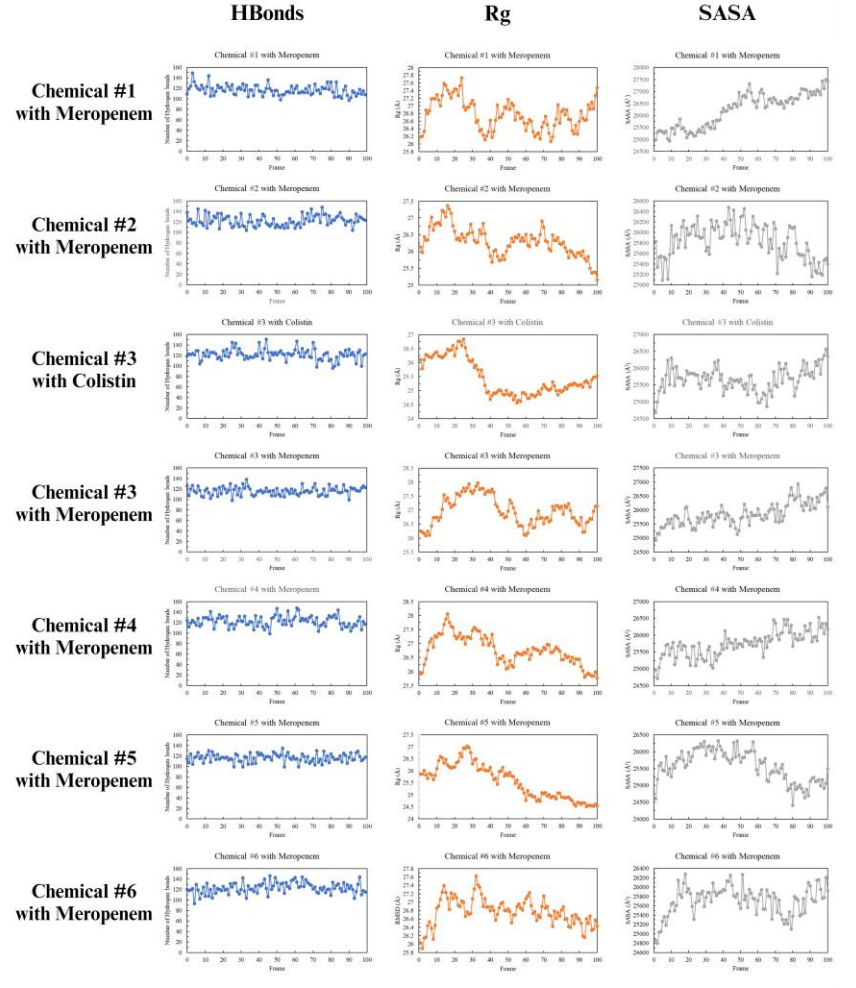

Figure 30. Post MD analysis. Plots for intramolecular hydrogen bond (Number of hydrogen bond vs. Frame), radius of gyration (Rg vs. Frame), and solvent-accessible surface area (SASA vs. Frame) of 7 different complex. 100 frames is equal to 10 ns. (Contributed by Gyusik Kim and Johnathan Lin)

4. Discussion

This genome section enables us to study the evolutionary disposition of MDR K56. Yet the genomic DNA levels still do not explain the resistance phenotype of meropenem. Neither distinguished pathogenetic virulence factors were discovered in K56 to affect colonization or damage to the host. If they are protective antigens, they are usable for developing vaccines[101].

According to the transcriptomic analysis, colistin treatment has upregulation of the xylulokinase (KPHS_36020) in the carbohydrate metabolism (Figure 23). Specifically, it works in the fermentation[102] process, where xylulose is phosphorylated to xylulose 5-phosphate in the xylose isomerase pathway. For cell metabolism, D-arabinitol dehydrogenase (KPHS_36030) participate in oxidation of D-arabitol to D-xylulose[103], related to the pentose phosphate pathway. Fermentation produces ATP, but less than the Krebs cycle and electron transport chain. There are also changes in the cellular respiration process to obtain energy under cell surface stress.

A gene expression graph in real-time qPCR (RT-qPCR) supports the RNAseq results (Figure 24). In real-time qPCR and ATP measurement experiments, the same trend was observed, but statistically, it is not significant. The quantity difference of KPHS_36020 among K56_Co (Colistin treatment), K56 only (Control), K56_Ch (Chemical #3 treatment), and K56_Co_Che (Colistin and Chemical #3 treatment) is not much, despite the fact that the fact that the experimental results were matched with the gene expression of the transcriptome.

Particularly in the colistin-only condition, an increase in carbon availability occurs without permeability-related changes in the phospholipids of the cell membrane.

A wavy double-layered membrane of gram-negative bacteria contains a thin peptidoglycan layer (https://wikipedia.org). These bacteria produce lipopolysaccharides, which act as endotoxins. Hence, to invade gram-negative bacteria, the cell envelope is an essential part of disruption. The chemical #3 physiochemical property may cause an intense reaction with the antibiotic colistin. The conflicting interplay of cell surface disruption and metabolic alterations is crucial for balancing the combination treatment's impact with bacterial homeostasis. This study's supporting data suggests that lysine breakdown, starch and sucrose metabolism, glycolysis, or gluconeogenesis protect the delicate bacteria's surface from the combination treatment. Carbohydrates, a component of peptidoglycans, are important for energy storage as well as cell envelope integrity[104] in bacteria. Reduced glycosyltransferase activity and glycosidic bond formation are achieved by lowered carbohydrate production. Furthermore, metabolisms of tyrosine and phenylalanine affect energy shortages, whereas changes in fatty acid content cause alterations in membrane phospholipid characteristics.

As part of the K56's survival strategy, not only carbon metabolism but also starch and sucrose metabolism get involved in energy generation under antimicrobial pressure. As a mechanism of virulence, bacterial infections include protein secretion into the extracellular environment with T2SS[105]. During T2SS secretion, cobalt ions enhance the activity of pullulanase[106]. Cobalamin

biosynthesis functions as a cofactor that regulates gene expression[107]. Porphyrin metabolism promotes the production of cobalamin. KPHS_42460 works in the declining cobalamin biosynthesis[108]. Both KPHS_42480 and KPHS_42640 relate to facilitated amidation in cobalamin biosynthesis[109]. These genes intensify gene expression under aerobic conditions in the late step of cobalt insertion and under anaerobic conditions in the first step of cobalt insertion[110]. Lower KPHS_11300 expression results in a decreasing heme biosynthetic process.

The phenylalanine leader peptide RNA thermometer has implications for nutrition and energy control, although additional research is needed to determine its exact significance. This depends on a harsh temperature or hunger condition to regulate expression[111] by modifing the secondary structure and causing exposure to the ribosome binding site[112]. Ultimately, it influences translation.

Investigating the activity of novel sRNAs and their interactions with the target gene KPHS_28070 is another option (Figure 22). Antisense sRNAs suppress sRNA activity by adhering to them before they interact with target mRNAs[113]. Therefore, gene expression is increasing due to less translational repression[114]. The use of a general stress protein (KPHS_28070) has potential for a future therapeutic strategy based on particular nucleotide sequences to regulate metabolism[115].

Riboswitches are essential regulatory regions of mRNA. They bind to tiny molecules via their aptamer domains for regulation. The existence or nonexistence of the ligand regulates gene expression. For example, the lysine riboswitch controls lysine production by inversely affecting citrate synthase activity in the

tricarboxylic acid cycle (https://rfam.org). Thus, the lysine riboswitch could be one of the most useful methods to remotely modulate bacterial cell growth. Because of its bacteria-specificity, cobalamin riboswitch also has the potential for a wide range of applications. The riboswitch requires interaction with the cobalamin transporter (KPHS_01080) for therapeutic administration. The functionally related genes that constitute a systemic network are regulated by these regulatory RNA elements throughout this process.

For survival, the secretion-specific[116] molecular chaperone[117] TF has functions in the prevention of misfolded and aggregated proteins[118] by interacting with the ribosome[119]. Likewise, it plays a role in bacterial virulence as a regulator[117,120].

Uronate isomerase catalyzes D-galacturonate and D-glucuronate pathways for conversion to D-tagaturonate and D-fructuronate, respectively[121]. In the catabolic process, pyruvate and 3-phosphoglyceraldehyde are the end products[122]. Besides the involvement of carbohydrate metabolism, the accumulation of pyruvate causes acid resistance in bacteria[123]. The acidic stress-related gene KPHS_28070 is targeted by novel sRNA from transcriptome analysis. Its movement protects bacteria from bacteriostasis. Thus, carbohydrate-related metabolic linking is obtained to prevent a cell surface alteration.

The most abundant[124] EF-Tu is the multidomain G protein, which participates as a substrate[124] in post-translational modifications such as inhibition[125]. During the translational elongation, the catalyzer binds aminoacyl-transfer RNA (aa-tRNA) to the A-site of the ribosome[126]. It also acts as a translation initiation factor

to maintain bacterial cell shape[127]. The bacterial outer membrane contributes to the mechanical strength of Gram-negative bacterial cell shape[128].

Beta-lactamase SHV (sulf-hydryl variable active site)[129] causes resistance to beta-lactam antibiotics[130], which are classified into penicillin, cephalosporins, carbapenems, and monobactams[131]. It is found frequently in *Klebsiella pneumoniae*[132]. The differences in the amino acid lead to a configurational alternation in the active site[131].

The genomic portion examined the evolution of the multidrug-resistant K56. K56's developmental alterations likely led to greater antibiotic resistance, higher plasmid copy numbers for horizontal transmission, and decreased cell division or binary fission for reproduction[133]. The toxin-antitoxin system is linked to stable plasmid inheritance proteins. The maltoporin lamB transporter serves as a receptor for recognizing lambda phages[134].

KPHS_02600 was chosen over KPHS_41450 due to its more well-documented traits and functionalities. KPHS_02600 is considerably overexpressed and consists of trimeric chains containing active sites. Porins on the outer membrane contribute to antibiotic resistance[135]. Both genes, located on the outer membrane, transport maltose and maltodextrins (https://uniprot.org). KPHS_41450 is also referred to as a maltose-inducible porin or lambda receptor protein. The presence of KPHS_41450 in K56 significantly increases the formation of KPHS_02600 in chemical #3 with colistin, which synergizes the reaction.

Molecular docking is a strong *in-silico* drug development approach. Low-affinity ligands are effective antibacterial agents[136]. Negative binding affinity values lead to more stable protein-ligand complexes (Figure 28). The disparity between experimental and computational results could be due to ligand concentration-dependent binding affinity. Combining chemical #3 with colistin promotes maltoporin, altering K56 metabolism. Antibiotic resistance has been linked to isolates with low lamB (maltoporin) activity[137].

Physicochemical parameters are employed to analyze compound features, bioactivity, and quantitative structure-activity correlations[45]. Structure diversity was evaluated using physicochemical characteristics and fingerprints. The physiochemical qualities determine the size, flexibility, and molecular polarity[138] of chemical space. The area makes it easier to study how chemical structures influence biological activity[139].

For chemical #3 with colistin, it has a high RMSD, but it was stable after a 5 ns simulation. Definitely, multiple 10 ns molecular dynamics (MD) simulations or 200 ns long MD simulation are required for reliable interpretation. In particular, we chose the second option to reach system equilibrium and protein-ligand complex convergence[140]. The possible reason for the high values is that the 10 ns simulation is too short for equilibrium; it could be just equilibration artifacts. Also, poor docking quality in the protein-multiple ligand complex, such as a deviated docking position, is another possible reason. The third potential reason is the complexity of the molecular system. We did not use a single ligand for each condition; it was multiple ligands.

Throughout this investigation, we proposed five viable ways for combating MDR K56. The multidisciplinary approaches include combination treatment (colistin and chemical #3), RNA regulators (RNA thermometer, riboswitch, and novel sRNA), target genes (KPHS_31750, KPHS_01080, KPHS_02470, and KPHS_28070), structural analog chemical compounds with optimization (chemical #1, chemical #2, chemical #3, chemical #4, chemical #5, and chemical #6), and maltoporin (KPHS_02600 and KPHS_41450). Additional research is necessary to determine whether these candidates are in therapeutic windows. For example, *in vivo* toxicity studies, biotechnology, the CRISPR Cas system, and MM-PBSA or MM-GBSA will validate our suggestions while also improving the quality of possible candidates.

5. Conclusion

A broader investigation range is necessary to define the mechanism of MDR K56 with K56_Co_Che combination treatment. Assumably, homeostasis is a defense to survive stressful conditions. The study set colistin and chemical #3 combination treatment as a starting point for potential therapeutics against MDR Klebsiella pneumoniae. The mechanism of the novel therapy and the bacterial survival strategy are unraveled by elucidating an intricate functional network with a comprehensive analysis. Specific pathways and noncoding RNAs are identified, and their interactions are discovered through systematic interpretation. Comparing the proteomic analysis at the protein level with both genome analysis at the DNA level and transcriptome analysis at the RNA level are more likely extended explorations with connections for supporting beta-lactam resistance genes, carbohydrate metabolism with acidic resistance, and cell shape maintenance with a translation initiation factor. K56, a multidrug-resistant strain, demonstrated resistance to several combinations of drugs. Likewise, this research examines antibiotic drug discovery by combining bioinformatics and cheminformatics technologies. The computational results suggest interactions between several ligands and distinct maltoporin proteins. Finding analogs of top candidates compounds can speed up the finding of a lead compound. One possible future research direction is to optimize them. Modifying bacterial genomes[141] with CRISPR Cas9 (gene off) and modified Cas9 (gene on) is also a promising approach for using these candidates as therapeutic methods. To validate the potential candidates, advanced investigation in fields such as synthetic biology,

pharmacology, and biotechnology is needed. This brief period of MD simulation provided us with insight into the dynamic relationship in spite of further investigation needed for filtering and computational findings validation, such as MM-PBSA or MM-GBSA binding free energy estimation. Nevertheless, the study discovers novel treatment options and builds a foundation for future research addressing antibiotic resistance.

References

1. Vading M, Nauclér P, Kalin M, Giske CG. Invasive infection caused by Klebsiella pneumoniae is a disease affecting patients with high comorbidity and associated with high long-term mortality. *PLoS One.* 2018;13(4):e0195258.
2. Lee M, Pinto NA, Kim CY, Yang S, D'Souza R, Yong D, et al. Network Integrative Genomic and Transcriptomic Analysis of Carbapenem-Resistant Klebsiella pneumoniae Strains Identifies Genes for Antibiotic Resistance and Virulence. *mSystems.* 2019;4(4).
3. Florensa AF, Kaas RS, Clausen P, Aytan-Aktug D, Aarestrup FM. ResFinder - an open online resource for identification of antimicrobial resistance genes in next-generation sequencing data and prediction of phenotypes from genotypes. *Microb Genom.* 2022;8(1).
4. Coleman SR, Blimkie T, Falsafi R, Hancock REW. Multidrug Adaptive Resistance of Pseudomonas aeruginosa Swarming Cells. *Antimicrob Agents Chemother.* 2020;64(3).
5. Andrade FF, Silva D, Rodrigues A, Pina-Vaz C. Colistin Update on Its Mechanism of Action and Resistance, Present and Future Challenges. *Microorganisms.* 2020;8(11).
6. Wolinsky E, Hines JD. Neurotoxic and nephrotoxic effects of colistin in patients with renal disease. *N Engl J Med.* 1962;266:759-762.
7. Brennan-Krohn T, Pironti A, Kirby JE. Synergistic Activity of Colistin-Containing Combinations against Colistin-Resistant Enterobacteriaceae. *Antimicrob Agents Chemother.* 2018;62(10).

8. Yu SH, Vogel J, Förstner KU. ANNOgesic: a Swiss army knife for the RNA-seq based annotation of bacterial/archaeal genomes. *Gigascience.* 2018;7(9).
9. Oliva G, Sahr T, Buchrieser C. Small RNAs, 5' UTR elements and RNA-binding proteins in intracellular bacteria: impact on metabolism and virulence. *FEMS Microbiol Rev.* 2015;39(3):331-349.
10. Dersch P, Laub M. Editorial overview: Cell regulation: New insights into the versatile regulatory processes governing bacterial life. *Curr Opin Microbiol.* 2017;36:v-viii.
11. Gygi SP, Corthals GL, Zhang Y, Rochon Y, Aebersold R. Evaluation of two-dimensional gel electrophoresis-based proteome analysis technology. *Proc Natl Acad Sci U S A.* 2000;97(17):9390-9395.
12. Harper S, Mozdzanowski J, Speicher D. Two-dimensional gel electrophoresis. *Curr Protoc Cell Biol.* 2001;Chapter 6:Unit 6.4.
13. Parker CE, Warren MR, Mocanu V. Frontiers in Neuroscience Mass Spectrometry for Proteomics. In: Alzate O, ed. *Neuroproteomics*. CRC Press/Taylor & Francis Copyright © 2010 by Taylor and Francis Group, LLC.; 2010.
14. Oselusi SO, Christoffels A, Egieyeh SA. Cheminformatic Characterization of Natural Antimicrobial Products for the Development of New Lead Compounds. *Molecules.* 2021;26(13).
15. Wang J, Yang W, Zhang S, Hu H, Yuan Y, Dong J, et al. A pangenome analysis pipeline provides insights into functional gene identification in rice. *Genome Biol.* 2023;24(1):19.

16. Sitto F, Battistuzzi FU. Estimating Pangenomes with Roary. *Mol Biol Evol.* 2020;37(3):933-939.
17. Raslan MA, Raslan SA, Shehata EM, Mahmoud AS, Sabri NA. Advances in the Applications of Bioinformatics and Chemoinformatics. *Pharmaceuticals (Basel).* 2023;16(7).
18. Palmer N, Maasch J, Torres MDT, de la Fuente-Nunez C. Molecular Dynamics for Antimicrobial Peptide Discovery. *Infect Immun.* 2021;89(4).
19. Melo MCR, Bernardi RC, de la Fuente-Nunez C, Luthey-Schulten Z. Generalized correlation-based dynamical network analysis: a new high-performance approach for identifying allosteric communications in molecular dynamics trajectories. *J Chem Phys.* 2020;153(13):134104.
20. Aminpour M, Montemagno C, Tuszynski JA. An Overview of Molecular Modeling for Drug Discovery with Specific Illustrative Examples of Applications. *Molecules.* 2019;24(9).
21. Wick RR, Schultz MB, Zobel J, Holt KE. Bandage: interactive visualization of de novo genome assemblies. *Bioinformatics.* 2015;31(20):3350-3352.
22. Alikhan NF, Petty NK, Ben Zakour NL, Beatson SA. BLAST Ring Image Generator (BRIG): simple prokaryote genome comparisons. *BMC Genomics.* 2011;12:402.
23. Martin M. Cutadapt removes adapter sequences from high-throughput sequencing reads. *EMBnet. journal.* 2011;17(1):10-12.
24. Bolger AM, Lohse M, Usadel B. Trimmomatic: a flexible trimmer for

Illumina sequence data. *Bioinformatics.* 2014;30(15):2114-2120.

25. Andrews S. *FastQC: a quality control tool for high throughput sequence data*. Babraham Bioinformatics, Babraham Institute; 2010.
26. Kim D, Paggi JM, Park C, Bennett C, Salzberg SL. Graph-based genome alignment and genotyping with HISAT2 and HISAT-genotype. *Nat Biotechnol.* 2019;37(8):907-915.
27. Kovaka S, Zimin AV, Pertea GM, Razaghi R, Salzberg SL, Pertea M. Transcriptome assembly from long-read RNA-seq alignments with StringTie2. *Genome Biol.* 2019;20(1):1-13.
28. Gim J, Won S, Park T. LPEseq: local-pooled-error test for RNA sequencing experiments with a small number of replicates. *PLoS One.* 2016;11(8):e0159182.
29. Förstner KU, Vogel J, Sharma CM. READemption-a tool for the computational analysis of deep-sequencing-based transcriptome data. *Bioinformatics.* 2014;30(23):3421-3423.
30. Shannon P, Markiel A, Ozier O, Baliga NS, Wang JT, Ramage D, et al. Cytoscape: a software environment for integrated models of biomolecular interaction networks. *Genome Res.* 2003;13(11):2498-2504.
31. Tyanova S, Temu T, Sinitcyn P, Carlson A, Hein MY, Geiger T, et al. The Perseus computational platform for comprehensive analysis of (prote)omics data. *Nat Methods.* 2016;13(9):731-740.
32. Oliveros J. Venny 2.1. 0. An interactive tool for comparing lists with Venn's diagrams. *BioinfoGP of CNB-CSIC.* 2015.

33. Park KS, Kim H, Kim NG, Cho SY, Choi KH, Seong JK, et al. Proteomic analysis and molecular characterization of tissue ferritin light chain in hepatocellular carcinoma. *Hepatology.* 2002;35(6):1459-1466.
34. Huynh ML, Russell P, Walsh B. Tryptic digestion of in-gel proteins for mass spectrometry analysis. *Methods Mol Biol.* 2009;519:507-513.
35. Lee HJ, Jeong SK, Na K, Lee MJ, Lee SH, Lim JS, et al. Comprehensive genome-wide proteomic analysis of human placental tissue for the Chromosome-Centric Human Proteome Project. *J Proteome Res.* 2013;12(6):2458-2466.
36. Seemann T. Prokka: rapid prokaryotic genome annotation. *Bioinformatics.* 2014;30(14):2068-2069.
37. Page AJ, Cummins CA, Hunt M, Wong VK, Reuter S, Holden MT, et al. Roary: rapid large-scale prokaryote pan genome analysis. *Bioinformatics.* 2015;31(22):3691-3693.
38. Junk P, Kiel C. HOMELETTE: a unified interface to homology modelling software. *Bioinformatics.* 2022;38(6):1749-1751.
39. Eberhardt J, Santos-Martins D, Tillack AF, Forli S. AutoDock Vina 1.2.0: New Docking Methods, Expanded Force Field, and Python Bindings. *J Chem Inf Model.* 2021;61(8):3891-3898.
40. Trott O, Olson AJ. AutoDock Vina: improving the speed and accuracy of docking with a new scoring function, efficient optimization, and multithreading. *J Comput Chem.* 2010;31(2):455-461.
41. O'Boyle NM, Banck M, James CA, Morley C, Vandermeersch T, Hutchison GR. Open Babel: An open chemical toolbox. *J Cheminform.*

2011;3:33.

42. Krivák R, Hoksza D. P2Rank: machine learning based tool for rapid and accurate prediction of ligand binding sites from protein structure. *J Cheminform.* 2018;10(1):39.

43. Laskowski RA, Swindells MB. LigPlot+: multiple ligand-protein interaction diagrams for drug discovery. *J Chem Inf Model.* 2011;51(10):2778-2786.

44. Xiong G, Wu Z, Yi J, Fu L, Yang Z, Hsieh C, et al. ADMETlab 2.0: an integrated online platform for accurate and comprehensive predictions of ADMET properties. *Nucleic Acids Res.* 2021;49(W1):W5-w14.

45. Backman TW, Cao Y, Girke T. ChemMine tools: an online service for analyzing and clustering small molecules. *Nucleic Acids Res.* 2011;39(Web Server issue):W486-491.

46. Reynolds TB. Strategies for acquiring the phospholipid metabolite inositol in pathogenic bacteria, fungi and protozoa: making it and taking it. *Microbiology (Reading).* 2009;155(Pt 5):1386-1396.

47. Deutscher J, Francke C, Postma PW. How phosphotransferase system-related protein phosphorylation regulates carbohydrate metabolism in bacteria. *Microbiol Mol Biol Rev.* 2006;70(4):939-1031.

48. Hooppaw AJ, McGuffey JC, Di Venanzio G, Ortiz-Marquez JC, Weber BS, Lightly TJ, et al. The Phenylacetic Acid Catabolic Pathway Regulates Antibiotic and Oxidative Stress Responses in Acinetobacter. *MBio.* 2022;13(3):e0186321.

49. Chimento DP, Mohanty AK, Kadner RJ, Wiener MC. Substrate-induced

transmembrane signaling in the cobalamin transporter BtuB. *Nat Struct Biol.* 2003;10(5):394-401.

50. Di Masi DR, White JC, Schnaitman CA, Bradbeer C. Transport of vitamin B12 in Escherichia coli: common receptor sites for vitamin B12 and the E colicins on the outer membrane of the cell envelope. *J Bacteriol.* 1973;115(2):506-513.
51. Bradbeer C, Woodrow ML, Khalifah LI. Transport of vitamin B12 in Escherichia coli: common receptor system for vitamin B12 and bacteriophage BF23 on the outer membrane of the cell envelope. *J Bacteriol.* 1976;125(3):1032-1039.
52. Korotkov KV, Sandkvist M. Architecture, Function, and Substrates of the Type II Secretion System. *Ecosal Plus.* 2019;8(2).
53. Naskar S, Hohl M, Tassinari M, Low HH. The structure and mechanism of the bacterial type II secretion system. *Mol Microbiol.* 2021;115(3):412-424.
54. Iwobi A, Heesemann J, Garcia E, Igwe E, Noelting C, Rakin A. Novel virulence-associated type II secretion system unique to high-pathogenicity Yersinia enterocolitica. *Infect Immun.* 2003;71(4):1872-1879.
55. Salmond GP, Reeves PJ. Membrane traffic wardens and protein secretion in gram-negative bacteria. *Trends Biochem Sci.* 1993;18(1):7-12.
56. Wandersman C, Delepelaire P, Letoffe S, Ghigo JM. A signal peptide-independent protein secretion pathway. *Antonie van Leeuwenhoek.*

1992;61(2):111-113.

57. Lory S. Determinants of extracellular protein secretion in gram-negative bacteria. *J Bacteriol.* 1992;174(11):3423-3428.

58. Howard SP, Critch J, Bedi A. Isolation and analysis of eight exe genes and their involvement in extracellular protein secretion and outer membrane assembly in Aeromonas hydrophila. *J Bacteriol.* 1993;175(20):6695-6703.

59. Sagulenko E, Sagulenko V, Chen J, Christie PJ. Role of Agrobacterium VirB11 ATPase in T-pilus assembly and substrate selection. *J Bacteriol.* 2001;183(20):5813-5825.

60. Sandkvist M, Hough LP, Bagdasarian MM, Bagdasarian M. Direct interaction of the EpsL and EpsM proteins of the general secretion apparatus in Vibrio cholerae. *J Bacteriol.* 1999;181(10):3129-3135.

61. Ferrández A, Miñambres B, García B, Olivera ER, Luengo JM, García JL, et al. Catabolism of phenylacetic acid in Escherichia coli. Characterization of a new aerobic hybrid pathway. *J Biol Chem.* 1998;273(40):25974-25986.

62. Nordlund I, Powlowski J, Shingler V. Complete nucleotide sequence and polypeptide analysis of multicomponent phenol hydroxylase from Pseudomonas sp. strain CF600. *J Bacteriol.* 1990;172(12):6826-6833.

63. Sherman BT, Hao M, Qiu J, Jiao X, Baseler MW, Lane HC, et al. DAVID: a web server for functional enrichment analysis and functional annotation of gene lists (2021 update). *Nucleic Acids Res.* 2022;50(W1):W216-w221.

64. Huang da W, Sherman BT, Lempicki RA. Systematic and integrative analysis of large gene lists using DAVID bioinformatics resources. *Nat Protoc.* 2009;4(1):44-57.

65. Muirhead H. Isoenzymes of pyruvate kinase. *Biochem Soc Trans.* 1990;18(2):193-196.

66. Kraft L, Sprenger GA, Lindqvist Y. Crystallization and preliminary X-ray crystallographic studies of recombinant thermoresistant gluconate kinase GntK from Escherichia coli. *Acta Crystallogr D Biol Crystallogr.* 2001;57(Pt 8):1159-1161.

67. Kraft L, Sprenger GA, Lindqvist Y. Conformational changes during the catalytic cycle of gluconate kinase as revealed by X-ray crystallography. *J Mol Biol.* 2002;318(4):1057-1069.

68. Izu H, Adachi O, Yamada M. Purification and characterization of the Escherichia coli thermoresistant glucokinase encoded by the gntK gene. *FEBS Lett.* 1996;394(1):14-16.

69. Lolis E, Petsko GA. Crystallographic analysis of the complex between triosephosphate isomerase and 2-phosphoglycolate at 2.5-A resolution: implications for catalysis. *Biochemistry.* 1990;29(28):6619-6625.

70. Kawada-Matsuo M, Oogai Y, Komatsuzawa H. Sugar Allocation to Metabolic Pathways is Tightly Regulated and Affects the Virulence of Streptococcus mutans. *Genes (Basel).* 2016;8(1).

71. Konkit M, Choi WJ, Kim W. Aldehyde dehydrogenase activity in Lactococcus chungangensis: Application in cream cheese to reduce aldehyde in alcohol metabolism. *J Dairy Sci.* 2016;99(3):1755-1761.

72. Whitworth DE, Morgan BH. Synergism Between Bacterial GAPDH and OMVs: Disparate Mechanisms but Co-Operative Action. *Front Microbiol.* 2015;6:1231.

73. Hackert ML, Carroll DW, Davidson L, Kim SO, Momany C, Vaaler GL, et al. Sequence of ornithine decarboxylase from Lactobacillus sp. strain 30a. *J Bacteriol.* 1994;176(23):7391-7394.

74. Janssen U, Fink T, Lichter P, Stoffel W. Human mitochondrial 3,2-trans-enoyl-CoA isomerase (DCI): gene structure and localization to chromosome 16p13.3. *Genomics.* 1994;23(1):223-228.

75. Rodionov DG, Ishiguro EE. Dependence of peptidoglycan metabolism on phospholipid synthesis during growth of Escherichia coli. *Microbiology (N Y).* 1996;142(10):2871-2877.

76. Robbe-Saule V, Lopes MD, Kolb A, Norel F. Physiological effects of Crl in Salmonella are modulated by sigmaS level and promoter specificity. *J Bacteriol.* 2007;189(8):2976-2987.

77. Rao KN, Kumaran D, Seetharaman J, Bonanno JB, Burley SK, Swaminathan S. Crystal structure of trehalose-6-phosphate phosphatase-related protein: biochemical and biological implications. *Protein Sci.* 2006;15(7):1735-1744.

78. Bren A, Park JO, Towbin BD, Dekel E, Rabinowitz JD, Alon U. Glucose becomes one of the worst carbon sources for E.coli on poor nitrogen sources due to suboptimal levels of cAMP. *Sci Rep.* 2016;6:24834.

79. Ruhal R, Kataria R, Choudhury B. Trends in bacterial trehalose

metabolism and significant nodes of metabolic pathway in the direction of trehalose accumulation. *Microb Biotechnol.* 2013;6(5):493-502.

80. Reizer J, Sutrina SL, Wu LF, Deutscher J, Reddy P, Saier MH, Jr. Functional interactions between proteins of the phosphoenolpyruvate:sugar phosphotransferase systems of Bacillus subtilis and Escherichia coli. *J Biol Chem.* 1992;267(13):9158-9169.
81. Postma PW, Lengeler JW, Jacobson GR. Phosphoenolpyruvate:carbohydrate phosphotransferase systems of bacteria. *Microbiol Rev.* 1993;57(3):543-594.
82. Hii SL, Tan JS, Ling TC, Ariff AB. Pullulanase: role in starch hydrolysis and potential industrial applications. *Enzyme Res.* 2012;2012:921362.
83. Szklarczyk D, Gable AL, Nastou KC, Lyon D, Kirsch R, Pyysalo S, et al. The STRING database in 2021: customizable protein-protein networks, and functional characterization of user-uploaded gene/measurement sets. *Nucleic Acids Res.* 2021;49(D1):D605-d612.
84. Wenlock MC, Barton P. In silico physicochemical parameter predictions. *Mol Pharm.* 2013;10(4):1224-1235.
85. Lagorce D, Douguet D, Miteva MA, Villoutreix BO. Computational analysis of calculated physicochemical and ADMET properties of protein-protein interaction inhibitors. *Sci Rep.* 2017;7:46277.
86. Fernandes J, Gattass CR. Topological polar surface area defines substrate transport by multidrug resistance associated protein 1 (MRP1/ABCC1). *J Med Chem.* 2009;52(4):1214-1218.

87. Riniker S, Landrum GA. Similarity maps - a visualization strategy for molecular fingerprints and machine-learning methods. *J Cheminform.* 2013;5(1):43.

88. Kumar S, Dubey R, Mishra R, Gupta S, Dwivedi VD, Ray S, et al. Repurposing of SARS-CoV-2 compounds against Marburg Virus using MD simulation, mm/GBSA, PCA analysis, and free energy landscape. *J Biomol Struct Dyn.* 2024:1-20.

89. Knapp B, Frantal S, Cibena M, Schreiner W, Bauer P. Is an intuitive convergence definition of molecular dynamics simulations solely based on the root mean square deviation possible? *J Comput Biol.* 2011;18(8):997-1005.

90. Bibi S, Khan MS, El-Kafrawy SA, Alandijany TA, El-Daly MM, Yousafi Q, et al. Virtual screening and molecular dynamics simulation analysis of Forsythoside A as a plant-derived inhibitor of SARS-CoV-2 3CLpro. *Saudi Pharm J.* 2022;30(7):979-1002.

91. Tallei TE, Fatimawali, Yelnetty A, Idroes R, Kusumawaty D, Emran TB, et al. An Analysis Based on Molecular Docking and Molecular Dynamics Simulation Study of Bromelain as Anti-SARS-CoV-2 Variants. *Front Pharmacol.* 2021;12:717757.

92. Sepay N, Sekar A, Halder UC, Alarifi A, Afzal M. Anti-COVID-19 terpenoid from marine sources: A docking, admet and molecular dynamics study. *J Mol Struct.* 2021;1228:129433.

93. Kumari R, Dhankhar P, Dalal V. Structure-based mimicking of hydroxylated biphenyl congeners (OHPCBs) for human transthyretin,

an important enzyme of thyroid hormone system. *J Mol Graph Model.* 2021;105:107870.

94. Yamamoto E, Akimoto T, Mitsutake A, Metzler R. Universal Relation between Instantaneous Diffusivity and Radius of Gyration of Proteins in Aqueous Solution. *Phys Rev Lett.* 2021;126(12):128101.
95. Mollaamin F, Layali I, Ilkhani A, Monajjemi M. Nanomolecular simulation of the voltage–gated potassium channel protein by gyration radius study. *Afr J Microbiol Res.* 2011;4:2795-2803.
96. Raman APS, Singh MB, Vishvakarma VK, Jain P, Kumar A, Sachdeva S, et al. An investigation for the interaction of gamma oryzanol with the Mpro of SARS-CoV-2 to combat COVID-19: DFT, molecular docking, ADME and molecular dynamics simulations. *J Biomol Struct Dyn.* 2023;41(5):1919-1929.
97. Boroujeni M, Shahbazi M, Shokrgozar MA, Rahimi H, Omidinia E. Computational driven molecular dynamics simulation of Keratinocyte Growth Factor behavior at different pH conditions. *Inform Med Unlocked.* 2021;23:100514.
98. Zhang D, Lazim R. Application of conventional molecular dynamics simulation in evaluating the stability of apomyoglobin in urea solution. *Sci Rep.* 2017;7:44651.
99. Gorai S, Junghare V, Kundu K, Gharui S, Kumar M, Patro BS, et al. Synthesis of Dihydrobenzofuro[3,2-b]chromenes as Potential 3CLpro Inhibitors of SARS-CoV-2: A Molecular Docking and Molecular Dynamics Study. *ChemMedChem.* 2022;17(8):e202100782.

100. Lee Y, Lee JJ, Kim S, Lee SC, Han J, Heu W, et al. Dissecting the critical factors for thermodynamic stability of modular proteins using molecular modeling approach. *PLoS One.* 2014;9(5):e98243.
101. He Y. Chapter 20 - Bacterial Whole-Genome Determination and Applications. In: Tang Y-W, Sussman M, Liu D, Poxton I, Schwartzman J, eds. *Molecular Medical Microbiology (Second Edition)*. Academic Press; 2015:357-368.
102. Zheng Z, Lin X, Jiang T, Ye W, Ouyang J. Genomic analysis of a xylose operon and characterization of novel xylose isomerase and xylulokinase from Bacillus coagulans NL01. *Biotechnol Lett.* 2016;38(8):1331-1339.
103. Cheng H, Jiang N, Shen A, Feng Y. Molecular cloning and functional expression of d-arabitol dehydrogenase gene from Gluconobacter oxydans in Escherichia coli. *FEMS Microbiol Lett.* 2005;252(1):35-42.
104. Kato K, Ishiwa A. The role of carbohydrates in infection strategies of enteric pathogens. *Trop Med Health.* 2015;43(1):41-52.
105. Sandkvist M. Type II secretion and pathogenesis. *Infect Immun.* 2001;69(6):3523-3535.
106. Wei W, Ma J, Chen SQ, Cai XH, Wei DZ. A novel cold-adapted type I pullulanase of Paenibacillus polymyxa Nws-pp2: in vivo functional expression and biochemical characterization of glucans hydrolyzates analysis. *BMC Biotechnol.* 2015;15:96.
107. Rowley CA, Kendall MM. To B12 or not to B12: Five questions on the role of cobalamin in host-microbial interactions. *PLoS Pathog.* 2019;15(1):e1007479.

108. Friedmann HC, Harris DL. THE FORMATION OF ALPHA-GLYCOSIDIC 5'-NUCLEOTIDES BY A SINGLE DISPLACEMENT TRANS-N-GLYCOSIDASE. *J Biol Chem.* 1965;240:406-412.

109. Blanche F, Couder M, Debussche L, Thibaut D, Cameron B, Crouzet J. Biosynthesis of vitamin B12: stepwise amidation of carboxyl groups b, d, e, and g of cobyrinic acid a,c-diamide is catalyzed by one enzyme in Pseudomonas denitrificans. *J Bacteriol.* 1991;173(19):6046-6051.

110. Moore SJ, Lawrence AD, Biedendieck R, Deery E, Frank S, Howard MJ, et al. Elucidation of the anaerobic pathway for the corrin component of cobalamin (vitamin B12). *Proc Natl Acad Sci U S A.* 2013;110(37):14906-14911.

111. Narberhaus F, Waldminghaus T, Chowdhury S. RNA thermometers. *FEMS Microbiol Rev.* 2006;30(1):3-16.

112. Narberhaus F. Translational control of bacterial heat shock and virulence genes by temperature-sensing mRNAs. *RNA Biol.* 2010;7(1):84-89.

113. Grosshans H, Filipowicz W. Molecular biology: the expanding world of small RNAs. *Nature.* 2008;451(7177):414-416.

114. Papenfort K, Vanderpool CK. Target activation by regulatory RNAs in bacteria. *FEMS Microbiol Rev.* 2015;39(3):362-378.

115. Rodrigo G, Prakash S, Cordero T, Kushwaha M, Jaramillo A. Functionalization of an antisense small RNA. *J Mol Biol.* 2016;428(5):889-892.

116. Valent QA, Kendall DA, High S, Kusters R, Oudega B, Luirink J. Early

events in preprotein recognition in E. coli: interaction of SRP and trigger factor with nascent polypeptides. *EMBO J.* 1995;14(22):5494-5505.

117. Wen ZT, Suntharaligham P, Cvitkovitch DG, Burne RA. Trigger factor in Streptococcus mutans is involved in stress tolerance, competence development, and biofilm formation. *Infect Immun.* 2005;73(1):219-225.

118. Matavacas J, Hallgren J, von Wachenfeldt C. Bacillus subtilis forms twisted cells with cell wall integrity defects upon removal of the molecular chaperones DnaK and trigger factor. *Front Microbiol.* 2022;13:988768.

119. Hoffmann A, Bukau B, Kramer G. Structure and function of the molecular chaperone Trigger Factor. *Biochim Biophys Acta.* 2010;1803(6):650-661.

120. Henderson B, Allan E, Coates AR. Stress wars: the direct role of host and bacterial molecular chaperones in bacterial infection. *Infect Immun.* 2006;74(7):3693-3706.

121. Nguyen TT, Fedorov AA, Williams L, Fedorov EV, Li Y, Xu C, et al. The mechanism of the reaction catalyzed by uronate isomerase illustrates how an isomerase may have evolved from a hydrolase within the amidohydrolase superfamily. *Biochemistry.* 2009;48(37):8879-8890.

122. Kuivanen J, Biz A, Richard P. Microbial hexuronate catabolism in biotechnology. *AMB Express.* 2019;9(1):16.

123. Wu J, Li Y, Cai Z, Jin Y. Pyruvate-associated acid resistance in bacteria.

Appl Environ Microbiol. 2014;80(14):4108-4113.

124. Hughes D. Elongation Factors: Translation☆. *Reference Module in Life Sciences*. Elsevier; 2017.

125. Talavera A, Hendrix J, Versées W, Jurėnas D, Van Nerom K, Vandenberk N, et al. Phosphorylation decelerates conformational dynamics in bacterial translation elongation factors. *Sci Adv.* 2018;4(3):eaap9714.

126. Harvey KL, Jarocki VM, Charles IG, Djordjevic SP. The Diverse Functional Roles of Elongation Factor Tu (EF-Tu) in Microbial Pathogenesis. *Front Microbiol.* 2019;10:2351.

127. Defeu Soufo HJ, Reimold C, Linne U, Knust T, Gescher J, Graumann PL. Bacterial translation elongation factor EF-Tu interacts and colocalizes with actin-like MreB protein. *Proc Natl Acad Sci U S A.* 2010;107(7):3163-3168.

128. Fivenson EM, Rohs PDA, Vettiger A, Sardis MF, Torres G, Forchoh A, et al. A role for the Gram-negative outer membrane in bacterial shape determination. *Proc Natl Acad Sci U S A.* 2023;120(35):e2301987120.

129. Zaniani FR, Meshkat Z, Naderi Nasab M, Khaje-Karamadini M, Ghazvini K, Rezaee A, et al. The Prevalence of TEM and SHV Genes among Extended-Spectrum Beta-Lactamases Producing Escherichia Coli and Klebsiella Pneumoniae. *Iran J Basic Med Sci.* 2012;15(1):654-660.

130. Leinberger DM, Grimm V, Rubtsova M, Weile J, Schröppel K, Wichelhaus TA, et al. Integrated detection of extended-spectrum-beta-

lactam resistance by DNA microarray-based genotyping of TEM, SHV, and CTX-M genes. *J Clin Microbiol.* 2010;48(2):460-471.

131. Liakopoulos A, Mevius D, Ceccarelli D. A Review of SHV Extended-Spectrum β-Lactamases: Neglected Yet Ubiquitous. *Front Microbiol.* 2016;7:1374.

132. AL-Subol I YN. Prevalence of CTX-M, TEM and SHV Beta-lactamases in Clinical Isolates of Escherichia Coli and Klebsiella Pneumoniae Isolated From Aleppo University Hospitals, Aleppo, Syria. . *Arch Clin Infect Dis.* 2015;10(2).

133. Dimitriu T, Matthews AC, Buckling A. Increased copy number couples the evolution of plasmid horizontal transmission and plasmid-encoded antibiotic resistance. *Proc Natl Acad Sci U S A.* 2021;118(31).

134. Berkane E, Orlik F, Charbit A, Danelon C, Fournier D, Benz R, et al. Nanopores: maltoporin channel as a sensor for maltodextrin and lambda-phage. *J Nanobiotechnology.* 2005;3(1):3.

135. Ghai I, Ghai S. Understanding antibiotic resistance via outer membrane permeability. *Infect Drug Resist.* 2018;11:523-530.

136. Akter T, Chakma M, Tanzina AY, Rumi MH, Shimu MSS, Saleh MA, et al. Curcumin Analogues as a Potential Drug against Antibiotic Resistant Protein, β-Lactamases and L, D-Transpeptidases Involved in Toxin Secretion in Salmonella typhi: A Computational Approach. *BioMedInformatics.* 2021;2(1):77-100.

137. Mishra M, Panda S, Barik S, Sarkar A, Singh DV, Mohapatra H. Antibiotic Resistance Profile, Outer Membrane Proteins, Virulence

Factors and Genome Sequence Analysis Reveal Clinical Isolates of Enterobacter Are Potential Pathogens Compared to Environmental Isolates. *Front Cell Infect Microbiol.* 2020;10:54.

138. Ahamed TKS, Muraleedharan K. A cheminformatic study on chemical space characterization and diversity analysis of 5-LOX inhibitors. *J Mol Graph Model.* 2020;100:107699.

139. Oselusi SO, Egieyeh SA, Christoffels A. Cheminformatic Profiling and Hit Prioritization of Natural Products with Activities against Methicillin-Resistant Staphylococcus aureus (MRSA). *Molecules.* 2021;26(12).

140. Ormeño F, General IJ. Convergence and equilibrium in molecular dynamics simulations. *Commun Chem.* 2024;7(1):26.

141. Arroyo-Olarte RD, Bravo Rodríguez R, Morales-Ríos E. Genome Editing in Bacteria: CRISPR-Cas and Beyond. *Microorganisms.* 2021;9(4).

Abstract in Korean

다제내성 폐렴막대균 발생과 연관된 유전자 네트워크

1980년대 이후로 다제내성균 치료를 위한 새로운 약물의 개발이 제한되면서 새로운 항생제의 필요성이 긴급히 대두되었습니다. 항생제 내성으로 인한 사망률 증가는 다른 주요 질병의 사망률을 능가하여 전 세계적으로 중요한 임상적 관심사가 되었습니다. 박테리아의 진화 속도는 미국 식품의약국(FDA)이 승인한 항생제의 개발 속도를 앞지르며, 이는 항생제 내성 위기를 심화시키고 전 세계 공중 보건에 해로운 영향을 미치며 의료 산업과 시스템에 상당한 경제적 손실을 초래하고 있습니다.

본 연구의 목적은 이전 실험 결과를 생물정보학 및 컴퓨터 기반 방법론의 결과와 비교하여 잠재적인 표적과 히트 화합물을 찾는 것입니다. 이를 달성하기 위한 전략으로 병용 요법을 적용하였습니다. 기존 약물의 용도 변경 또는 부분 용도 변경은 광범위한 작용 스펙트럼을 제공하며, 단일 요법에 비해 내성 발생 가능성을 감소시키고 다양한 균주에 효과적인 새로운 접근 방식을 제시하였습니다. 또한, 더 낮은 치료 용량으로도 실질적인 효능을 유지하여 부작용을 최소화할 수 있

었습니다.

ESKAPE 기회감염 병원체로 분류되는 *Klebsiella pneumoniae*는 병원과 지역사회 감염을 일으켜 위협이 됩니다. 본 연구에서는 ANNOgesic를 사용하여 전사 후 조절에 중요한 역할을 하는 noncoding RNA를 감지하고, 기능적 네트워크를 형성하는 다양한 경로와 riboswitch 및 RNA thermometer와 같은 규제 RNA 요소의 존재를 밝히며 그 관여도를 예측했습니다. 특정 유전자의 발현을 특징으로 하는 이러한 경로는 병용 요법의 치료 효과와 박테리아 생존 전략에 기여합니다. 경로 간의 연결은 환경 변화에 반응하는 regulatory RNA 요소에 의해 촉진됩니다. 이러한 발견은 가혹한 환경 조건에서 박테리아의 적응 반응을 시사합니다. 더욱이, 본 연구는 표적 유전자와 상호작용하는 새로운 small regulatory RNA의 존재를 찾아 잠재적인 항균 치료 후보를 발견하는 데 기여할 것입니다. 전반적으로, 본 연구는 박테리아 반응과 생존 전략에서 규제 RNA 요소의 역할을 강조하며, 화합물과 항생제의 시너지 효과에 대한 귀중한 통찰을 제공하였습니다. 새로운 noncoding RNA의 식별과 표적 유전자, riboswitch 및 RNA thermometer와의 상호작용은 항균 치료법 개발에 대한 가능성을 제시하였습니다.

또한, 히트 화합물 발견을 위한 물리적 및 화학적 성질과 유사도 분석, 단백질-다수 리간드 도킹 연구 과정을 설명하였습니다. 또한, 화합

물과 항생제 환경에 있는 시스템의 반응을 연구하기 위해 원자 간의 운동을 연구하는 분자 동역학 시뮬레이션을 도입했습니다. 그러나 10 ns 분자 동역학 시뮬레이션은 시스템 평형 및 단백질-리간드 복합체 형성을 위한 충분한 시간이 아니므로, 신뢰성을 높이기 위해 향후 200 ns의 분자 동역학 시뮬레이션, 사후 분석 및 MM-PBSA (Molecular Mechanics Poisson-Boltzmann Surface Area) 또는 MM-GBSA (Molecular Mechanics Generalized Born Surface Area) 결합 자유에너지 평가를 통해 후보 화합물을 필터링하여 히트 화합물을 찾고 잠재적인 유사 화합물 또한 고려하여 향후 연구의 후보 범위를 확장할 수 있었습니다. 앞으로 합성생물학, 약리학, 생명공학 등의 분야에서 추가 연구가 필요합니다. 이 연구를 통해 항생제 내성 문제를 해결하기 위한 향후 연구의 기반을 구축하였습니다.

핵심되는 말 : 다제내성, 메로페넘, 콜리스틴, 시너지 효과, ANNOgesic, noncoding RNA, 유전자 네트워크, 단백질 및 리간드 상호작용, 화학정보학, 분자동역학